The Astrophysical Journal Supplement Series, 277:6 (20pp), 2025 March https://doi.org/10.3847/1538-4365/ada3ba

Photometric Stellar Parameters for 195,478 Kepler Input Catalog Stars

Bowen Zhang[1,2], Yang Huang[1,2,4], Timothy C. Beers[3], Kai Xiao[2], Jifeng Liu[1,2], Lei Jia[1], Henggeng Han[1], Zhirui Li[1,2], Chuanjie Zheng[1,2], Yongkang Sun[1,2], Ruifeng Shi[2], and Hongrui Gu[1,2]
[1] Key Lab of Optical Astronomy, National Astronomical Observatories, Chinese Academy of Sciences, Beijing 100101, People's Republic of China; huangyang@ucas.ac.cn
[2] School of Astronomy and Space Science, University of Chinese Academy of Sciences, Beijing 100049, People's Republic of China
[3] Department of Physics and Astronomy and JINA Center for the Evolution of the Elements (JINA-CEE), University of Notre Dame, Notre Dame, IN 46556, USA
Received 2024 November 12; revised 2024 December 18; accepted 2024 December 20; published 2025 February 17

Abstract

The stellar atmospheric parameters and physical properties of stars in the Kepler Input Catalog (KIC) are of great significance for the study of exoplanets, stellar activity, and asteroseismology. However, despite extensive effort over the past decades, accurate spectroscopic estimates of these parameters are available for only about half of the stars in the full KIC. In our work, by training relationships between photometric colors and spectroscopic stellar parameters from Gaia DR3, the Kepler-INT Survey, Large Sky Area Multi-Object Fiber Spectroscopic Telescope DR10, and Galactic Evolution Experiment at Apache Point Observatory DR17, we have obtained atmospheric parameter estimates for over 195,000 stars, accounting for 97% of the total sample of KIC stars. We obtain 1σ uncertainties of 0.1 dex on metallicity [Fe/H], 100 K on effective temperature $T_{\rm eff}$, and 0.2 dex on surface gravity log g. In addition, based on these atmospheric parameters, we estimated the ages, masses, radii, and surface gravities of these stars using the commonly adopted isochrone-fitting approach. External comparisons indicate that the resulting precision for turnoff stars is 20% in age; for dwarf stars, it is 0.07 $M_{\odot}$ in mass, 0.05 $R_{\odot}$ in radius, and 0.12 dex in surface gravity; and for giant stars, it is 0.14 $M_{\odot}$ in mass, 0.73 $R_{\odot}$ in radius, and 0.11 dex in surface gravity.

Unified Astronomy Thesaurus concepts: Metallicity (1031); Fundamental parameters of stars (555); Stellar ages (1581); Sky surveys (1464)

1. Introduction

As the most powerful and successful exoplanet explorer to date, the Kepler/K2 mission (W. J. Borucki et al. 2010; S. B. Howell et al. 2014) has discovered more than 3300 exoplanets, over half of the currently confirmed exoplanets. The extremely precise and short-cadence (~1 minute) light curves obtained from Kepler/K2 have revolutionized the field of asteroseismology. These data have facilitated the detection of solar-like oscillations in over 500 main-sequence and subgiant stars (W. J. Chaplin et al. 2014), as well as for more than 20,000 red giants (e.g., D. Stello et al. 2013; J. Yu et al. 2016). This extensive data set has enabled accurate modeling of the fundamental properties of these stars across nearly the entire low-mass Hertzsprung–Russell (H-R) diagram (D. Huber & K. Zwintz 2020). There are also 75 exoplanets confirmed from Kepler's archival data, demonstrating the enduring impact and vitality of this space mission.

During its first 4 yr of operations, Kepler made long-term observations of the Kepler field, a 116 deg^2 area of sky located between the constellations Cygnus and Lyra. To guide these observations, a catalog of some 200,000 stars, known as the Kepler Input Catalog (KIC; T. M. Brown et al. 2011), was determined in advance. Observations of this area accumulated a large amount of photometric data over temporal baselines on the order of years, which have not only greatly advanced the field of exoplanet search and characterization but also provided an important basis for research in many other fields, including stellar activity, asteroseismology, and the study of star clusters (R. L. Gilliland et al. 2010; T. Shibayama et al. 2013; A. McQuillan et al. 2014; W. J. Borucki 2016).

The fundamental stellar parameters of stars play a important role in refining our understanding of stellar theoretical models and evolution. In order to construct the appropriate stellar models to constrain their evolution, the physical properties of stars, in particular the metallicity, are essential input parameters (C. A. Tremonti et al. 2004; A. Bressan et al. 2012). The situation is similar for the estimation of stellar ages and masses; a precise metallicity estimate of a star is required. After determining the stellar age, the age–rotation relation can be analyzed to a high level of precision (V. Witzke et al. 2020; K. Masuda 2022). The metallicity also deeply influences the stellar atmosphere and structure, as well as the relationship between stellar activity and metallicity (C. Karoff et al. 2018; V. See et al. 2023; V. Loaiza-Tacuri et al. 2024).

The nature of the exoplanet(s) associated with a star is expected to be related to the physical properties of the host. Both the probability that a star hosts a planet and the type of the planet are influenced by the elemental abundances of the protoplanetary disk (G. Gonzalez 1997; J. A. Johnson et al. 2010; E. A. Petigura et al. 2018; K. M. Boley et al. 2024). Furthermore, the radius gap, a region that shows a deficit of planet occupation in the planet radius–mass map (at around 1.9 $R_{\oplus}$), is also thought to be influenced by the host star's metallicity, mass, and age (E. D. Lopez & J. J. Fortney 2013; J. E. Owen & Y. Wu 2017; K. K. Hardegree-Ullman et al. 2020; R. Burn et al. 2024; S. Yun et al. 2024).

[4] Corresponding author.

Table 1
KIC Stars in Large-scale/Dedicated Spectroscopic Surveys

Catalog/Survey	Number
KIC	200,038
LAMOST DR10	79,015
APOGEE DR17	23,198
CKS DR1 and DR2	1716
KIC stars with spectroscopic parameters	86,482

However, we still lack full information on the fundamental stellar parameters of KIC stars, particularly metallicity, which is crucial for accurately determining other parameters as mentioned above. Attempts to obtain this information continued throughout the Kepler mission, both before and after. Prior to the launch of the Kepler satellite, the atmospheric parameters of KIC stars were estimated through the use of broadband photometry. For example, T. M. Brown et al. (2011) provided estimates of the metallicity, effective temperature, surface gravity, and extinction toward KIC stars using a Bayesian posterior estimation method based on this photometry. However, the stellar parameters predicted by this method differ significantly from those obtained from both low-resolution (e.g., S. Dong et al. 2014) and high-resolution spectroscopic studies with the Keck telescope (e.g., J. A. Johnson et al. 2017).

The Kepler Stellar Properties Catalog (D. Huber et al. 2014) provided revised stellar parameters for 138,600 targets in Quarters 1–16 (Q1–Q16), using colors, proper motions, spectroscopy, parallaxes, and Galactic population synthesis models. However, only 7% of stars in this catalog had spectroscopic information at that time. Applying similar methods, S. Mathur et al. (2017) provided stellar parameters for 197,096 targets in Quarters 1–17 (Q1–Q17). Again, spectroscopic parameters were available for no more than 10% of sample stars. Most recently, this group (T. A. Berger 2020) provided a catalog for 186,301 Kepler stars, with fundamental properties (including stellar ages) homogeneously estimated from isochrone fitting using broadband photometry, and Gaia Data Release 2 parallaxes, as well as spectroscopic metallicities if available. Compared to previous versions, the fraction of stars with spectroscopic information has increased to approximately 35% (about 66,000 stars), less than half of the number of KIC stars.

Another major effort for obtaining stellar parameters for KIC stars are large-scale spectroscopic surveys, including the Large Sky Area Multi-Object Fiber Spectroscopic Telescope (LAMOST)–Kepler Survey (P. De Cat et al. 2015; W. Zong et al. 2018; J.-N. Fu et al. 2020; J. Fu et al. 2022), the Galactic Evolution Experiment at Apache Point Observatory (APOGEE)–Kepler Survey (M. H. Pinsonneault et al. 2014; M. Pinsonneault et al. 2018), and the California-Kepler Survey (CKS; J. A. Johnson et al. 2017; E. A. Petigura et al. 2017, 2018). As shown in Table 1, these three surveys have obtained stellar parameters for 78,141, 23,198, and 1716 stars by cross-matching their data releases with the KIC. Despite these extensive efforts, the total number of stars with spectroscopically measured atmospheric parameters is 85,986, still less than 50% of the number of KIC stars.

More recently, stellar atmospheric and other physical parameters have been derived using narrow- or medium-band photometric surveys, particularly those in the near-ultraviolet bands (e.g., H. Yuan et al. 2015b; Y. Huang et al. 2019, 2022, 2023, 2024; A. Chiti et al. 2021). The precision is comparable to that achieved from low- or medium-resolution spectroscopy. In recent decades, the Kepler field has been observed using near-ultraviolet bands, such as the Kepler-INT Survey (KIS; S. Greiss et al. 2012a, 2012b), or through the use of Gaia XP spectra. Parameter-sensitive narrow- or medium-band photometric colors (e.g., the well-known Strömgren filter system) can be readily integrated from the flux-calibrated low-resolution spectra (LRS) of the latter survey. In this work, we aim to determine stellar parameters for all KIC stars using narrow- or medium-band photometric colors from these surveys, with spectroscopic labels from the LAMOST serving as training data. The paper is structured as follows: Section 2 describes the data. Section 3 presents the 3D extinction map toward the Kepler field. Atmospheric parameters are determined in Section 4, while physical parameters are estimated in Section 5. Finally, Sections 6 and 7 provide a discussion and a summary.

2. Data

The Kepler field, a 116 deg^2 region situated between Cygnus and Lyra, is centered at celestial coordinates (α, δ) = (290°, 45°) and Galactic coordinates (l, b) = (76°, 14°) (T. M. Brown et al. 2011) and has attracted a multitude of surveys. In this work, we primarily employed data from Gaia Data Release 3, KIS Data Release 2, Large Sky Area Multi-Object Fiber Spectroscopic Telescope Data Release 10, and Apache Point Observatory Galactic Evolution Experiment Data Release 17, supplemented with distance estimates sourced from the catalog by C. A. L. Bailer-Jones et al. (2021).

2.1. Gaia DR3

The Gaia third data release (DR3; Gaia Collaboration et al. 2023), derived from observations over a 35-month period, not only includes low-resolution ($R = \lambda/\Delta\lambda \sim 50$) BP/RP (XP) spectra for around 220 million sources, predominantly those with magnitudes brighter than $G < 17.65$ (well calibrated both internally and externally by J. M. Carrasco et al. 2021, F. De Angeli et al. 2023, and P. Montegriffo 2023, respectively), but also offers the most precise photometric data (G, BP, RP) to date for approximately 1.8 billion stars (Gaia Collaboration et al. 2021a, 2021b; M. Riello 2021). This provides the high-quality photometric and slitless spectroscopic data essential for conducting our study.

Based on the Gaia XP spectra, we further synthesized Strömgren photometry for the *vby* bands using the generation function provided by the Python package `GaiaXPy` (D. Ruz-Mieres & zuzannakr 2022).

2.2. KIS DR2

The Kepler field is observed by the KIS (S. Greiss et al. 2012a, 2012b), which employs the Isaac Newton Telescope (INT) to collect photometric data. The KIS second data release (DR2) includes U-, g-, r-, i-, and Hα-band photometry for 14.5 million stars, spanning a 113 deg^2 area of the Kepler field. In particular, the near-violet U-band photometry in KIS DR2 is crucial for the analysis presented in this work.

2.3. LAMOST DR10

LAMOST features a unique quasi-meridian reflecting Schmidt design outfitted with 4000 optical fibers, covering a 20 deg^2 field of view. Its 10th data release (DR10) provides an extensive collection of tens of millions of low-resolution ($R \sim 1800$) spectra across the optical spectrum from 3800 to 9000 Å. For estimation of the primary stellar atmospheric parameters (effective temperature $T_{\rm eff}$, surface gravity log g, and metallicity [Fe/H]), the project relies on the LAMOST Stellar Parameter Pipeline for AFGK stars (LASP; Y. Wu et al. 2011; Y. Wu et al. 2014) and LAMOST Stellar Parameter Pipeline for M stars (LASPM; B. Du et al. 2021).

2.4. APOGEE DR17

APOGEE, as a part of the Sloan Digital Sky Survey (SDSS-III) initiative, aimed to comprehensively address galaxy formation by conducting an unprecedented large-scale survey with detailed chemical and kinematic analysis. The APOGEE Stellar Parameter and Chemical Abundances Pipeline (ASPCAP; A. E. Garcìa Pérez et al. 2016) delivers high-precision estimates of stellar parameters, including effective $T_{\rm eff}$, surface gravity log g, and metallicity [Fe/H]. APOGEE DR17 published stellar atmosphere parameters for about 0.73 million stars, achieving measurement precision of typically 2%, 0.1 dex, and 0.05 dex for $T_{\rm eff}$, log g, and [Fe/H], respectively.

In this work, we utilized both photometric and spectroscopic data to estimate the atmospheric parameters of KIC stars. To achieve this, we crossmatched the KIC with data from the aforementioned surveys. After crossmatching, we found 199,571 stars with Gaia DR3 ultra−wide-band photometry, 197,157 stars with Gaia DR3 XP spectra, and 190,604 stars with KIS DR2 photometry. For spectroscopic data, we found 23,198 stars observed by APOGEE and 79,015 observed by LAMOST, as summarized in Table 1. To incorporate extinction values from the map derived in Section 3, we required distance estimates for the KIC stars. Crossmatching with C. A. L. Bailer-Jones et al. (2021) provided distance information for 197,064 stars. All crossmatching processes were conducted using TopCat (M. B. Taylor 2005), employing the best-matching model and a 3″ matching radius.

3. Construction of a 3D Dust Map for the Kepler Field with the "Star-pair" Method

In this study, the D. J. Schlegel et al. (1998) dust map $E(B-V)$ is not utilized for reddening correction, due to its inadequacies at low Galactic latitudes and the presence of spatially dependent errors, as reported in recent work by Sun et al. (2022). Instead, the 3D dust map for the Kepler field, derived through the straightforward "star-pair" (SP) method (H. B. Yuan et al. 2013; see their Section 5 for more details), is employed.

The central idea behind the SP method is that stars with similar atmospheric parameters—metallicity, effective temperature, and surface gravity—exhibit analogous intrinsic colors. The SP method typically involves defining the relationship between the intrinsic colors and the physical quantities using a sample of low-extinction stars, which is then applied to the entire sample to obtain $E(\mathrm{BP}-\mathrm{RP})$.

A detailed description of the SP method with the Gaia DR3 photometry color BP − RP and LAMOST DR10 spectroscopic stellar parameters is as follows.

1. We combine the Gaia DR3 photometric data with the spectroscopic data from LAMOST DR10, as well as the C. A. L. Bailer-Jones et al. (2021) distance catalog, with a crossmatching radius of 3″. A reference sample, constituting 1,037,145 stars, is selected with the following constraints: (1) signal-to-noise ratio for the g band (SNR_g) of the LAMOST spectra greater than 20; (2) Galactic latitude higher than 40°; (3) the 3D dust map from G. M. Green et al. (2019), represented as $E(B-V)_{\rm G19}$, is less than 0.01; and (4) C. A. L. Bailer-Jones et al. (2021) relative distance error less than 30%, in order to avoid poorly constrained distance information.
2. To construct the Kepler field target sample, we combine the Gaia DR3 photometric data with the spectroscopic data from LAMOST DR10, as well as the C. A. L. Bailer-Jones et al. (2021) distance catalog, with a crossmatching radius of 3″. The target sample includes 126,277 stars that meet the following constraints: (1) SNR_g of the LAMOST spectra more than 20, (2) located in the sky area where R.A. ranges from 279° to 302° and decl. ranges from 36° to 52°, and (3) C. A. L. Bailer-Jones et al. (2021) relative distance error less than 30%.
3. The BP − RP is adopted from the Gaia BP and RP bands; the intrinsic color $(\mathrm{BP}-\mathrm{RP})_0$ can be estimated from $(\mathrm{BP}-\mathrm{RP})_0 = \mathrm{BP}-\mathrm{RP}-E(\mathrm{BP}-\mathrm{RP})$. To obtain the reddening value, $E(\mathrm{BP}-\mathrm{RP})$, a transformation is performed as shown in the following equation:

$$E(\mathrm{BP}-\mathrm{RP}) = (R_{\rm BP}-R_{\rm RP})E(B-V)_{\rm G19}, \quad (1)$$

where $R_{\rm BP/RP}$ is the reddening coefficient with respect to $E(B-V)_{\rm G19}$ for the BP and RP bands, respectively, which can be calculated with

$$R_{\rm BP/RP} = R_V(A_{\rm BP/RP}/A_V), \quad (2)$$

where R_V represents the total-to-selective extinction ratio, defined as $R_V \equiv \frac{A_V}{E(B-V)}$. Here, instead of fixing it at 3.1, we use the actual measurements from R. Zhang et al. (2023) for each target. The $A_{\rm BP/RP}$ and A_V are the reddening values in the BP/RP and V bands, respectively. The reddening ratio of $A_{\rm BP/RP}/A_V$ is taken from S. Wang & X. Chen (2019).

For each target star, the reference stars are selected from the reference sample as those having values of $T_{\rm eff}$, log g, and [Fe/H] that differ from those of the target by less than 130 K, 0.06 dex, and 0.06 dex, respectively. The box sizes for selecting reference stars are empirically determined to ensure both a sufficient number of stars and a clear relationship between intrinsic color and atmospheric parameters within the box range. The extinction values for the target stars $E(\mathrm{BP}-\mathrm{RP})$ are measured from the difference between the observed color BP − RP and intrinsic color $(\mathrm{BP}-\mathrm{RP})_0$. The latter is derived both assuming that the intrinsic colors of the target and its control stars vary linearly with $T_{\rm eff}$, log g, and [Fe/H] and based on the random forest machine learning fitting technique (L. Breiman 2001). From comparison with the results of the above two techniques, the outcome of the random forest approach has been selected as the final result.

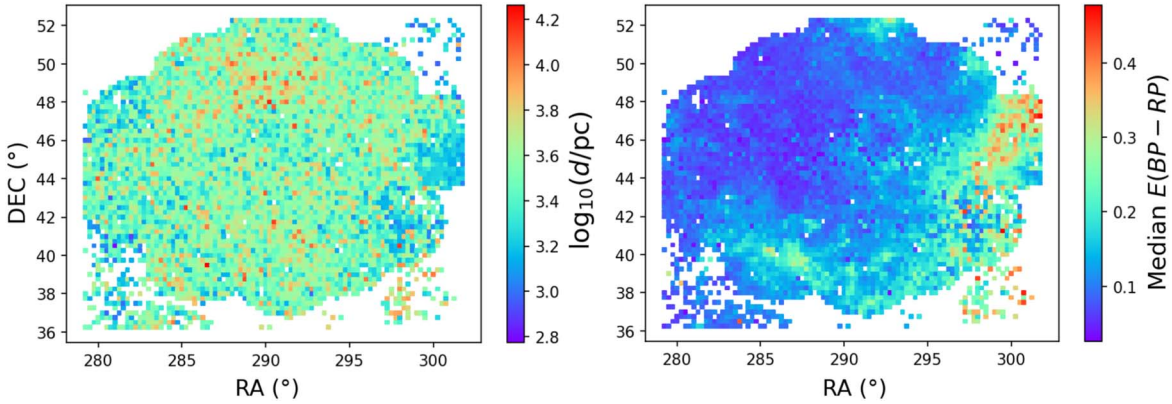

Figure 1. Depth (left panel) and median $E(B-V)$ (right panel) of the 3D reddening map toward Kepler field, coded by the color bars shown to the right of each panel.

4. To construct a continuous 3D extinction map applicable to all KIC stars, it is required to interpolate the discrete reddening values we have obtained. We subdivided the Kepler field into a grid of $10' \times 10'$ squares, assuming that the stars within each grid share the same line of sight. For the stars in each grid square, we employed two interpolation techniques: cubic function fitting and Gaussian error function fitting. We then derived continuous color-excess values. Among these two interpolation strategies, the method demonstrating superior goodness of fit, as measured by the coefficient of determination, was adopted as the final choice.

Finally, we constructed a 3D extinction map with an angular resolution of $10'$ and a distance resolution of 20 pc in the Kepler field, as shown in Figure 1. As a first check, the extinction values $E(\mathrm{BP}-\mathrm{RP})$ yielded by the SP method are directly compared with those from $E(B-V)_{\mathrm{G19}}$ (see Figure A1). Generally, they are very consistent with each other, with a negligible offset and a moderate scatter of 0.037 mag. We further assess the accuracy of reddening derived from the SP technique using member stars of open clusters, where extinction values are assumed to be constant. In the Kepler field, there are four open clusters: NGC 6811, NGC 6819, NGC 6866, and NGC 6791. Using positions, distances, and proper motions from Gaia DR3 (following the methods in Y. Huang et al. 2019; X.-Y. Li et al. 2023), we selected member stars of these four open clusters according to their mean positions, distances, and proper motions reported in C. A. L. Bailer-Jones et al. (2021), and E. L. Hunt & S. Reffert (2023). The extinction distributions $E(B-V)$ for the member stars, derived both from our SP technique and from G. M. Green et al. (2019), are shown in Figure A2. It is evident that the SP technique produces narrower distributions for all four clusters, indicating that the internal precision of the SP method is significantly higher than that of G. M. Green et al. (2019). Typically, the scatter in the extinction distributions obtained using the SP technique is significantly smaller than 0.01 mag, whereas the scatter from G. M. Green et al. (2019) exceeds 0.025 mag. The median extinction values for the member stars of all four clusters are consistent with those reported in the literature (see Table A1; K. Janes et al. 2013; B. J. Anthony-Twarog et al. 2014; D. Bossini et al. 2019).

4. Stellar Atmospheric Parameter Estimation

Multiband photometric data, particularly if narrowband filters are involved, provide an extremely efficient means to estimate stellar atmospheric parameters, as has been recognized for over half a century. For example, B. Strömgren (1963) first elucidated the relationship between narrow/medium-band photometric colors and stellar metallicity. As of today, the large-sample spectroscopic surveys, such as SDSS/SEGUE (B. Yanny et al. 2009; C. M. Rockosi et al. 2022), LAMOST, and APOGEE, provide excellent calibration labels for this method. H. Yuan et al. (2015a) obtained the typical relation between the width of stellar loci and the range of metallicity by analyzing spectroscopic stellar parameters and SDSS DR9 (C. P. Ahn et al. 2012) photometric data of Stripe 82. Following this, H. Yuan et al. (2015b) developed a method, based on fitting relationships between metallicity and photometric colors, and used this relationship to predict metallicity for stars with photometric colors but lacking spectroscopy. By adopting a similar method, Y. Huang et al. (2022) obtained atmospheric parameter estimates for over 20 million stars using SMSS DR2 photometric data and LAMOST DR9 and APOGEE DR17 spectroscopic data. Y. Huang et al. (2023) obtained stellar parameters for more than 20 million additional stars in the northern sky from the SAGES survey (Z. Fan et al. 2023). We here will adopt the same technique to derive metallicity, effective temperature, and surface gravity for KIC stars from the KIS and synthesized Strömgren photometry from Gaia XP spectra.

4.1. Metallicity

To derive photometric metallicity, we use stars in common with the LAMOST-KIC data set as our training set. In total, there are over 77,000 KIC stars observed by LAMOST with g-band SNR $\geqslant 20$. Using these training stars, we aim to establish relationships between spectroscopic metallicity and stellar colors taken from either the KIS or Strömgren photometry synthesized from Gaia XP spectra. Generally, the relationships are trained separately for dwarf and giant stars. To achieve better precision, we here train the relationships across five luminosity classes, including giants with $(\mathrm{BP}-\mathrm{RP})_0 < 1.8$, main-sequence stars with $(\mathrm{BP}-\mathrm{RP})_0 < 1.8$, binaries, turnoff stars, and blue stars with $(\mathrm{BP}-\mathrm{RP})_0 < 0.4$, based on their positions in the color–absolute magnitude diagram (see Figure 2). We note that the cuts to select these classes are empirically determined.

To show the sensitivities of KIS U and Strömgren $m_1 \equiv (v-b)-(b-y)$ on metallicity, two examples are shown in Figure 3 for main-sequence and giant stars. The plots clearly demonstrate sequences at different metallicities ranging from around $[\mathrm{Fe/H}] = -2.0$ to $[\mathrm{Fe/H}] = +0.5$, as both colors

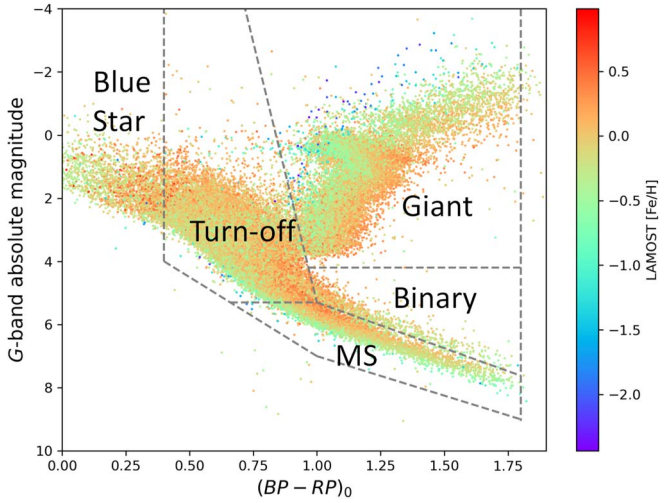

Figure 2. Color–absolute magnitude diagram of the training sample defined in Section 4.1, coded by LAMOST metallicity, as shown in color bar to the right. The dashed lines represent the cuts to separate different types of stars, i.e., the main-sequence (MS) stars, binary stars, giant stars, turnoff stars, and blue stars with $(\mathrm{BP}-\mathrm{RP})_0 < 0.40$.

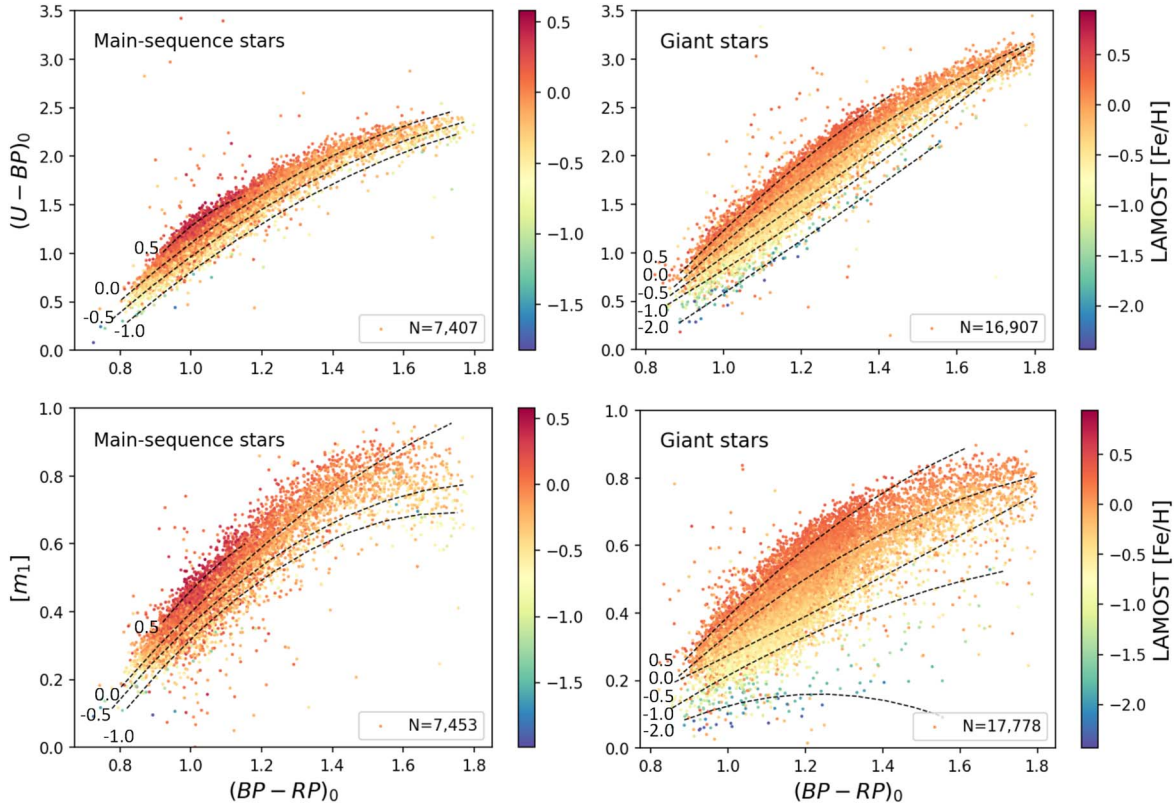

Figure 3. Distributions of the training-sample main-sequence stars (left panels) and giant stars (right panels) in the $(U-\mathrm{BP})_0$ vs. $(\mathrm{BP}-\mathrm{RP})_0$ plane (top panels) and the $[m_1]$ vs. $(\mathrm{BP}-\mathrm{RP})_0$ plane (bottom panels), coded by LAMOST metallicity ([Fe/H]), as shown by the color bars to the right of each panel. The dashed lines represent equal-metallicity sequences ranging from $+0.5$ (up) to -1.0 (bottom panel) for dwarf stars and $+0.5$ (up) to -2.0 (bottom panel) for giant stars. These sequences are obtained by fitting second-order polynomials to stars in the metallicity range $|[\mathrm{Fe/H}]-[\mathrm{Fe/H}]_i| < 0.1$, where $[\mathrm{Fe/H}]_i$ represents the marked metallicity of these sequences. The numbers of stars in each panel are provided in the lower right corner of the panel.

$(U-\mathrm{BP})_0$ and $[\mathrm{m_1}] \equiv (v-b)_0-(b-y)_0$ change with the BP for typical FGK-type stars.[5] Instead of using two-dimensional polynomial functions, as employed by previous studies (e.g., H. Yuan et al. 2015b; Y. Huang et al. 2022), we adopt the random forest machine learning method to model the relations $[\mathrm{Fe/H}] = f((U-\mathrm{BP})_0, (\mathrm{BP}-\mathrm{RP})_0)$ and $[\mathrm{Fe/H}] = f([m_1], (\mathrm{BP}-\mathrm{RP})_0)$ separately for the five luminosity classes.

After establishing the metallicity–color relations through training, we applied them to the entire KIC stellar sample to derive their photometric metallicities. In total, we derived photometric metallicities for 179,413 KIC stars using the model

[5] Here the reddening coefficients of the U and Strömgren bands are all taken from http://svo2.cab.inta-csic.es/theory/fps/.

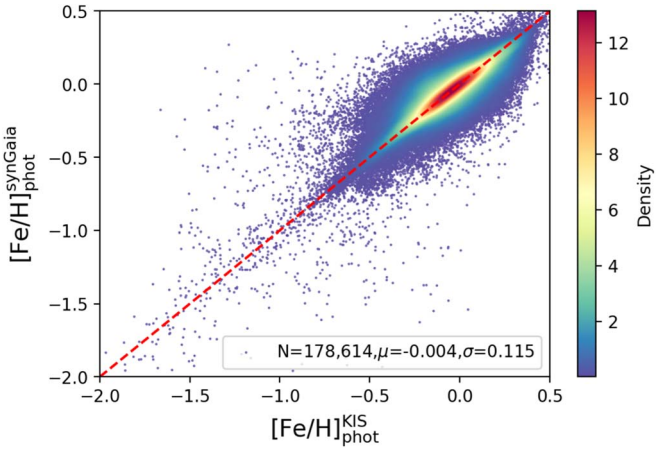

Figure 4. Comparison of photometric metallicity estimates derived from KIS photometry with those having synthesized Strömgren from Gaia XP spectra. The red dashed line is the one-to-one line. The color bar at right codes the number density of stars. The numbers of stars, mean offset, and dispersion are provided in the lower right corner.

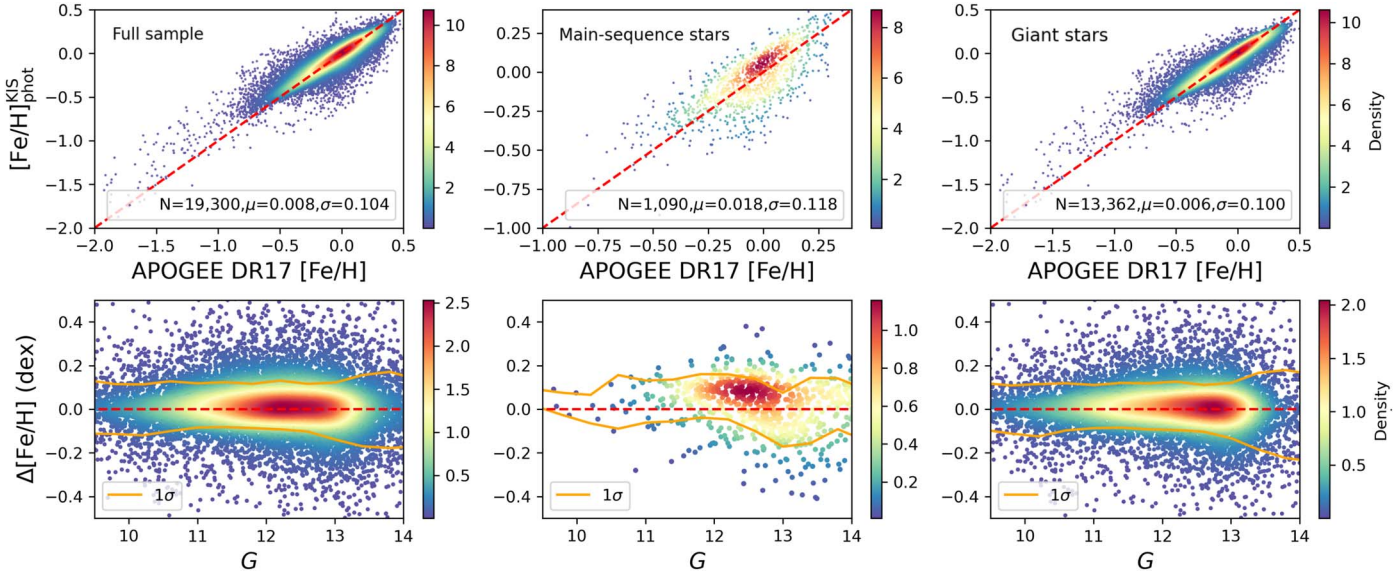

Figure 5. Top panels: comparison of photometric metallicity estimates from the KIS photometry with those from APOGEE DR17 for the full sample (left), main-sequence stars (middle), and giant stars (right). The red dashed lines are the one-to-one lines. The numbers of stars, mean offset, and dispersion are provided in the lower right corner of each panel. Bottom panels: residuals of the metallicity differences ($[Fe/H]_{phot} - [Fe/H]_{APOGEE}$), as a function of Gaia G magnitude. The red dashed line is the zero level. The golden lines represent the 1σ scatter. The color bar at the right of each panel codes the number density of stars.

trained with KIS photometry and for 189,727 stars using the model trained on Gaia XP spectral-synthesis-generated photometric data. Overall, this yields metallicity estimates for 191,551 stars, representing 95% of the total KIC stellar sample. First, as an internal check, the metallicity estimated from KIS is compared to that derived from the synthesized Strömgren photometry in Figure 4. No offset is found between the estimates from the two relations, with a minimal scatter of only 0.12 dex. This suggests an intrinsic precision of 0.08 dex, assuming equal contributions to the scatter from both relations.

To check the accuracy of the derived photometric metallicity, we crossmatched and compared KIC with results from APOGEE DR17. Overall, the photometric metallicities estimated from KIS and Strömgren colors exhibit excellent agreement with those from APOGEE DR17, with negligible offsets and a very small scatter of around 0.10 dex (see Figures 5 and 6). However, we find that the photometric metallicities are slightly higher than those from APOGEE DR17, likely due to differences in the metallicity scales between LAMOST and APOGEE (Y. Huang et al. 2024). This consistency holds across all stellar types, except for blue stars, where the limited number of KIC-APOGEE common stars prevents a meaningful comparison (see Figures 5, 6, B1, and B2). The precision for main-sequence, turnoff, giant, and binary stars is 0.12, 0.10, 0.10, and 0.18 dex, respectively.

To further evaluate the accuracy of the photometric metallicities, our sample is crossmatched with wide binaries selected from Gaia DR2 (H.-J. Tian et al. 2020), which are expected to have identical metallicities owing to their identical birthplace and formation time. In total, 131 and 144 wide binaries are found to have photometric estimates of metallicity measured from KIS and Strömgren colors,

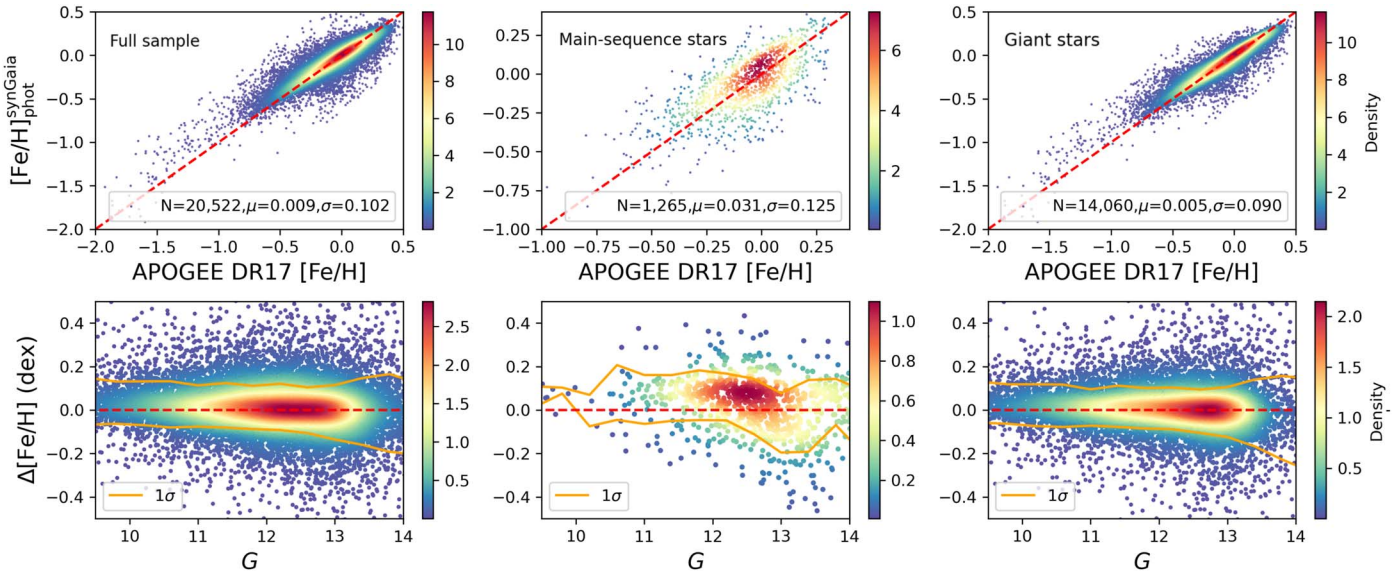

Figure 6. Similar to Figure 5, but for photometric metallicity estimates from Strömgren photometry synthesized from the Gaia XP spectra.

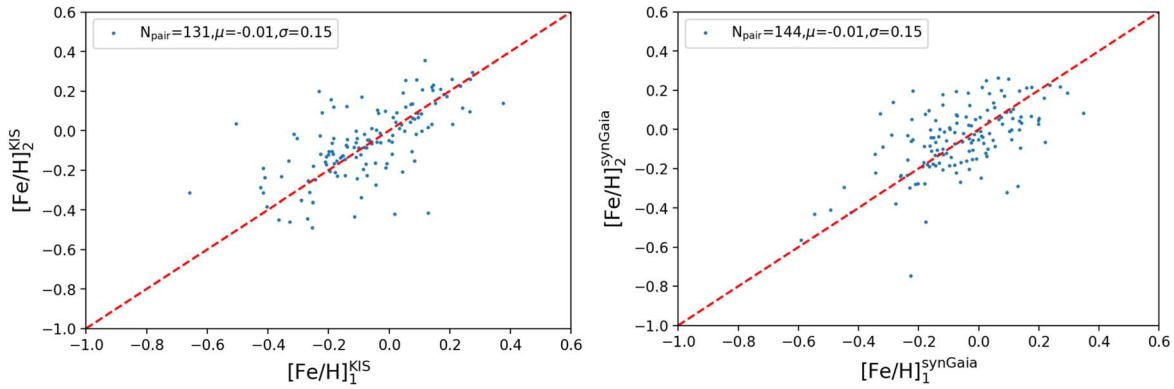

Figure 7. Comparison of photometric [Fe/H] estimates between wide binary members. Left panel: comparison of our method based on synthetic photometric data generated from Gaia XP spectra. Right panel: our method based on KIS photometric data. The red dashed lines are the one-to-one lines. The numbers of stars, mean offset, and dispersion are provided in the upper left corner of each panel.

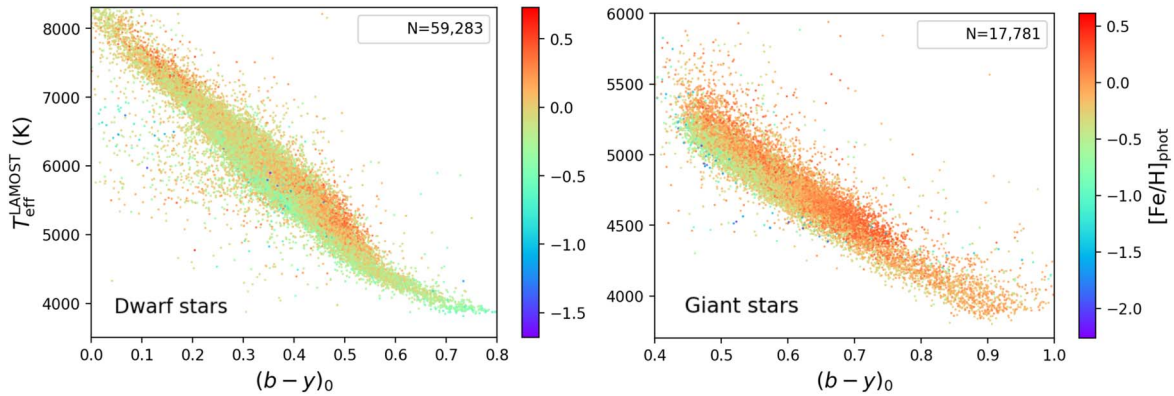

Figure 8. The relations between $T_{\rm eff}$ and color for dwarf stars (including main-sequence stars, turnoff stars, and blue stars, shown in the left panel) and giants (right panel). The $T_{\rm eff}$ data are adopted from LAMOST DR10, and the [Fe/H] data are from our photometric estimates. The numbers of stars are shown in the upper right corner of each panel. The color bar to the right of each panel codes the photometric metallicity estimates.

respectively. As shown in Figure 7, the offsets are within 0.02 dex, with a scatter of approximately 0.15 dex, demonstrating the consistency of metallicities between stars in the same binary system.

4.2. Effective Temperature

In the previous subsection, we discussed the methodology for estimating the photometric metallicity for the great majority

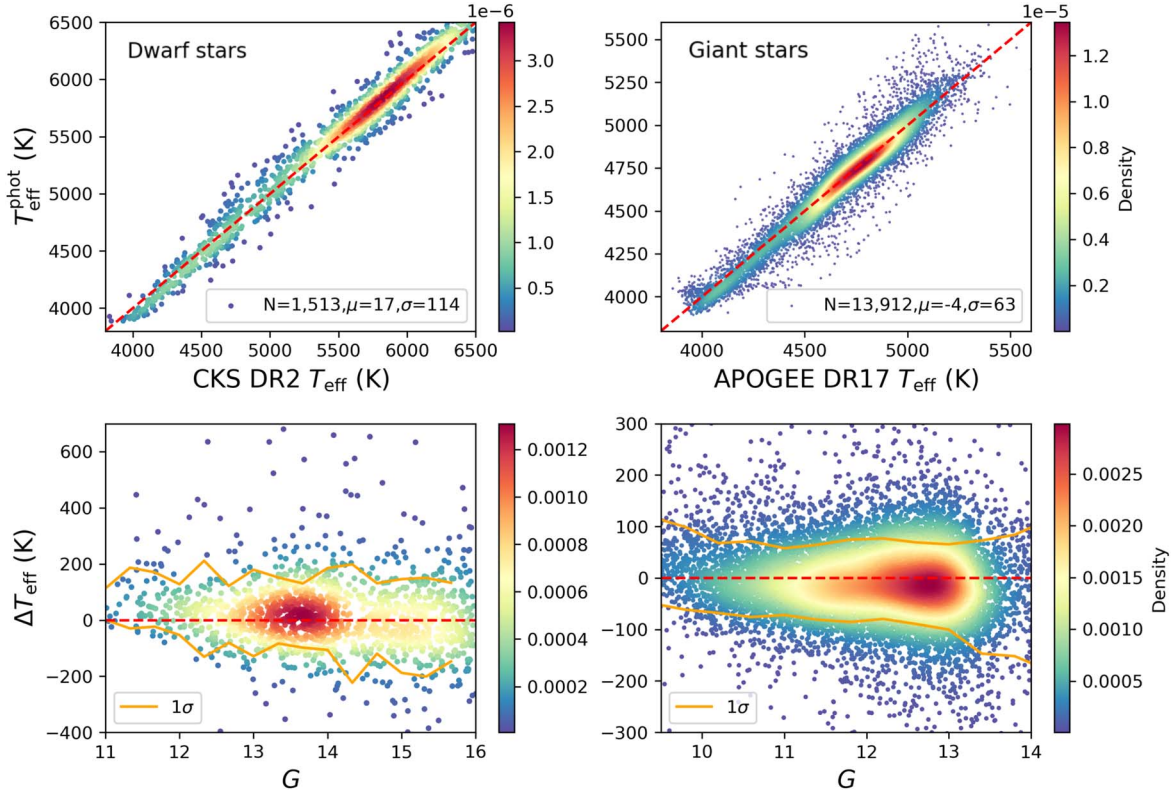

Figure 9. Comparison of $T_{\rm eff}$ obtained by our method with that from CKS DR2 (left panels, for dwarf stars) and APOGEE DR17 (right panels, for giant stars). The red dashed lines in the top panels are the one-to-one lines. The numbers of stars, mean offset, and dispersion are provided in the lower right corner of each panel in the top row. The bottom panels show the residuals in the sense of $T_{\rm eff}^{\rm phot} - T_{\rm eff}^{\rm APOGEE}$, as a function of G magnitude. The red dashed lines in the bottom panels represent the zero level. The golden lines in the bottom panels represents the 1σ scatter. The color bar to the right of each panel codes the number density of stars in the figure.

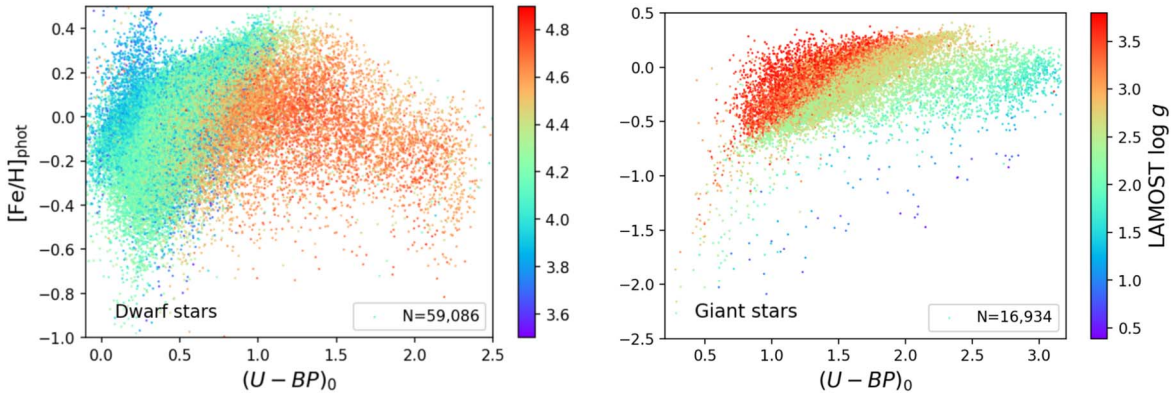

Figure 10. The relations between log $g-(U-BP)_0$ and photometric metallicity estimates for main-sequence stars (left panel) and giant stars (right panel). The log g data are from LAMOST DR10, and the metallicities are obtained by our photometric estimates. The numbers of stars are provided in the lower right corner of each panel. The color bar to the right of each panel codes the LAMOST DR10 estimate of log g.

of the KIC stars. These photometric metallicities will serve as inputs to the training sets for subsequent steps in this work. First, we consider the effective temperature, $T_{\rm eff}$.

Figure 8 shows the $T_{\rm eff}$ versus $(b-y)$ color plots for giants and dwarfs (hereafter dwarfs represent main-sequence stars, turnoff stars, and blue stars). In this case, the photometry is synthetically generated from the Gaia XP spectra, the effective temperatures are taken from the LAMOST DR10 spectroscopic data, and the metallicities used to color code the legend are those obtained from the photometric fits described in Section 4.1. From inspection, similar to the color–color map, the stars are on distinct loci and are stratified because of their different metallicities. We obtain estimates of effective temperature with the following relationship:

$$T_{{\rm eff},i} = f((b-y)_0, [{\rm Fe/H}]). \quad (3)$$

Again, a random forest regressor machine learning method is adopted to train the $T_{\rm eff}$–color–[Fe/H] relation. For the training set, the spectroscopic effective temperature is chosen from the LAMOST DR10 LRS AFGK catalog, with ${\rm SNR}_g > 20$. The total training set consists of 71,892 stars. In this section, we use a different division of stars compared to Section 4.1 to train the $T_{\rm eff}$–color–[Fe/H] relation separately. Here the stars are divided into three types, dwarfs, binaries, and giants, rather than the five types used in Section 4.1. After comparing the accuracy of the metallicities derived in Section 4.1 with the

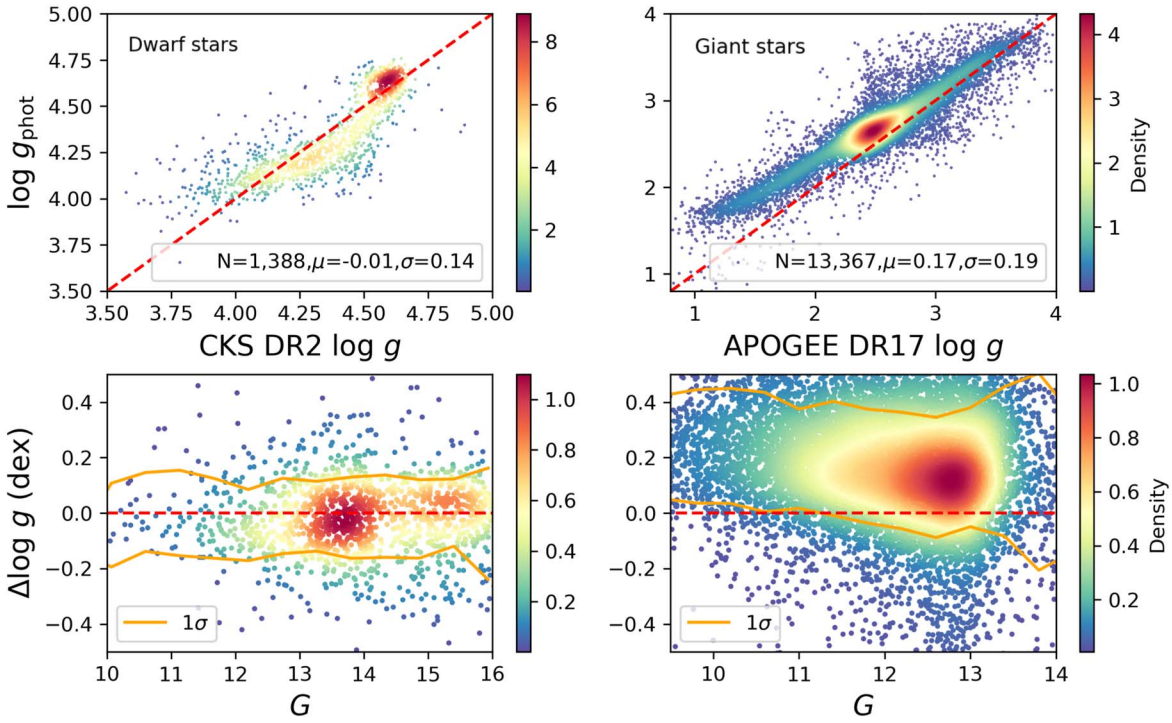

Figure 11. Comparison of log g estimates obtained by our method with CKS DR2 (left panels, for dwarf stars) and APOGEE DR17 (right panels, for giant stars). The red dashed lines in the top panels are the one-to-one lines. The numbers of stars, mean offset, and dispersion are provided in the lower right corner of each panel. The bottom panels show the residuals in the sense of $\log g_{\rm phot} - \log g_{\rm APOGEE/CKS}$, as a function of G magnitude. The red dashed lines in the bottom panels represent the zero level. The golden lines in the bottom panels represent the 1σ scatter. The color bar to the right of each panel codes the number density of stars in the panel.

APOGEE DR17 data, we adopted the photometric metallicity estimates from the method with higher accuracy for each type of star. For stars classed as dwarfs, the photometric metallicity estimates trained by KIS and Gaia photometry were adopted. For stars classed as binary or giant, we employed the photometric metallicities trained by synthetic photometry data from the Gaia XP spectra.

We then applied the trained relations to all three types of stars, resulting in effective temperature estimates for a total of 189,727 KIC stars. Figure 9 shows a comparison with the spectroscopic effective temperatures from CKS DR2 (E. A. Petigura et al. 2017, 2018) and APOGEE DR17. For the giant sample, there is a tiny offset of only +4 K and a dispersion of 63 K when analyzing the difference of our photometric $T_{\rm eff}$ minus APOGEE DR17. For the binaries, the offset is +110 K with a scatter of 247 K. For the dwarf sample, we compared our photometric $T_{\rm eff}$ estimates with those from CKS DR2, rather than APOGEE DR17, as the latter's pipeline is primarily designed for giant stars. The results show a small offset of +17 K (this work minus CKS) with a scatter of 114 K.

4.3. Surface Gravity

We now consider surface gravity estimates for the KIC stars based on the photometric color and photometric metallicities. Figure 10 shows the log g–$(U-{\rm BP})$ color plots for giant and dwarf stars. In this case, the photometry data are from KIS DR2 and Gaia DR3. The metallicities are from the result of photometric estimates as described in Section 4.1, and the surface gravities used for training are from the LAMOST DR10 spectroscopic data. The U-band photometry contains information about both the Balmer jump (which correlates with surface gravity) and metallicity. With the photometric metallicity fixed, the color $(U-{\rm BP})_0$ can be further used to constrain log g. As seen in the plots, the stars are stratified owing to their different values of log g. Once again, we employed a random forest regressor machine learning method to train the log g–color–[Fe/H] relations for different types of stars, following the same technical treatments as used for effective temperature (see Section 4.2). The total training set consists of 68,063 stars. From Figure 10, we note that, among the dwarf stars, some with low log g values, located at $(U-{\rm BP})_0 \sim 0.5$ and [Fe/H] ~ -0.6, do not conform to the overall log g gradient changes in the $(U-{\rm BP})_0$–$({\rm BP}-{\rm RP})_0$ diagram. Upon further examination, we found that these stars are located at the boundary between turnoff stars and subgiant stars. Therefore, the discrepancy for these stars is possibly due to their stellar classification; they are better classified as giants than as dwarfs. We then applied the trained relations to all types of stars, obtaining surface gravity estimates for 189,727 KIC stars. Figure 11 shows a comparison between our method and the spectroscopic surface gravity estimates from CKS DR2 (for dwarf stars) and APOGEE DR17 (for giants and binaries). The result for dwarfs exhibits an offset of −0.01 dex (this work minus CKS DR2) and a dispersion of 0.14 dex. As for the result for giant stars compared with APOGEE DR17, the offset is +0.17 dex (this work minus APOGEE DR17) and the dispersion is 0.19 dex. For binaries, the offset is +0.03 dex (this work minus APOGEE DR17) and the dispersion is 0.09 dex. The moderate offset in surface gravity for giant stars is primarily due to the scale difference between LAMOST (used as the training set) and APOGEE. By comparing over 10,000 common stars between LAMOST and APOGEE, we detected a similar offset of approximately 0.14 dex in surface gravity for giant stars.

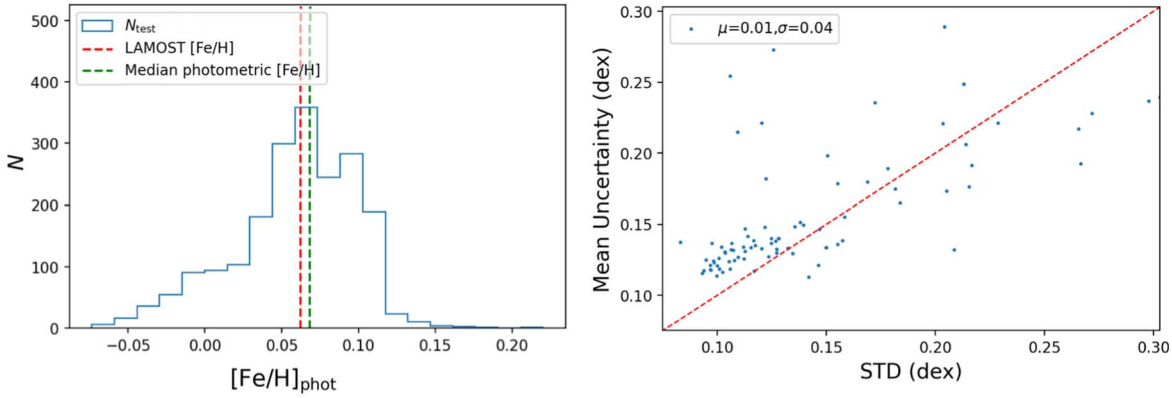

Figure 12. Left panel: an example of the distribution of final photometric estimates of [Fe/H] yielded by the MC simulations. The median value of this distribution is marked by a green dashed line, and the estimate by LAMOST is marked by a red dashed line. Right panel: comparison of the mean uncertainties derived from our MC method with those obtained from APOGEE DR17. The "STD" is estimated by calculating the dispersion of the metallicity difference between photometric method and APOGEE DR17 across various magnitude bins. We use 100 bins, evenly spaced between magnitudes 10 and 16. The red dashed line is the one-to-one line.

Table 2
Polynomial-fitting Coefficients for the Relationship between [α/Fe] and [Fe/H]

a_0	a_1	a_2	a_3	a_4	a_5	a_6
−0.0676	−0.3995	−0.6846	−0.1530	0.3205	−0.1469	0.0355

Note. $[\alpha/\mathrm{Fe}] = a_0 \times b^6 + a_1 \times b^5 + a_2 \times b^4 + a_3 \times b^3 + a_4 \times b^2 + a_5 \times b + a_6$ $b = [\mathrm{Fe/H}]$.

4.4. Uncertainty Analysis

Random forest machine learning methods generally do not provide uncertainty estimates for the derived parameters of individual stars. To address this, we estimate the uncertainty of each parameter using the Monte Carlo (MC) method. The MC simulation accounts for both the uncertainties in the input quantities and the mapping relations defined by the random forest regressor.

Using [Fe/H] as an example, we train the color–[Fe/H] relations with the random forest algorithm 1000 times. In each iteration, we sample the photometric errors from KIS/Gaia-synthesized photometry and Gaia data, as well as the uncertainties in extinction. All these errors are assumed to follow a Gaussian distribution. We then apply each relation to all KIC stars, again sampling their photometric and extinction uncertainties under the assumption of Gaussian distributions. For each star, this process yields a distribution of photometric [Fe/H], with the dispersion serving as the uncertainty. Figure 12 shows an example of the final distribution of 1000 simulated photometric [Fe/H] estimates and dispersion. Following the same approach, we derive the uncertainties for photometric $T_{\rm eff}$ and log g.

To validate the reliability of the uncertainty estimates, we compare our results with those from APOGEE DR17. First, we divide the stars into magnitude bins within the specified magnitude range. For each bin, we calculate the dispersion of the differences between our derived [Fe/H] and those from APOGEE DR17, treating this dispersion as the reference uncertainty for that group. Then, we compare these reference uncertainties with the mean uncertainties obtained from our method. As shown in the right panel of Figure 12, the uncertainties from the MC simulations are in excellent agreement with those with APOGEE DR17 uncertainties, with an offset of 0.01 dex and a dispersion of 0.04 dex, confirming the robustness of the uncertainty calculations.

5. Stellar Age Estimation

5.1. Bayesian Estimate

In this section, we derive ages, masses, and radii of the KIC stars from isochrone fitting based on a Bayesian approach. The methods we apply are similar to those used by B. R. Jørgensen & L. Lindegren (2005) and Y. Huang et al. (2022). Essentially, we match the observed parameters with the theoretical results given by stellar evolution models and obtain these estimates from the models.

The observed parameters we employ are (1) the intrinsic color $(\mathrm{BP}-\mathrm{RP})_0$ and G-band absolute magnitude of the KIC stars, corrected by our 3D extinction map; and (2) the stellar metallicities. For metallicity, we combined the spectroscopic metallicities from APOGEE and LAMOST, where available, along with the photometric metallicities obtained by our methods. For metallicities from different sources, we used the following criteria. For a given KIC star, if the APOGEE data have a metallicity that is obtained from a spectrum with SNR larger than 30, this metallicity is chosen. If this is not available and there is an available metallicity obtained from a LAMOST low-resolution spectrum whose g-band SNR is greater than 30, we select that estimate. If neither of these is available, we select the photometric metallicity using the same strategy employed for selecting data for the training set for models used to fit the $T_{\rm eff}$–color–[Fe/H] and log g–color–[Fe/H] relations, according to the assigned object type of the star.

For the stellar evolution models, we used the PARSEC isochrones (A. Bressan et al. 2012). For the ages and metallicities of the models, we divided the grid over the age ranging from 0.1 to 15.2 Gyr and [M/H] from −2.2 to +0.5. The step of the age grid is 0.2 Gyr for models with ages younger than 1.2 Gyr, and it is 0.5 Gyr for models whose ages are older than 1.2 Gyr. The step in [M/H] is 0.02 dex. This yields a grid of 1.38×10^6 stellar model points.

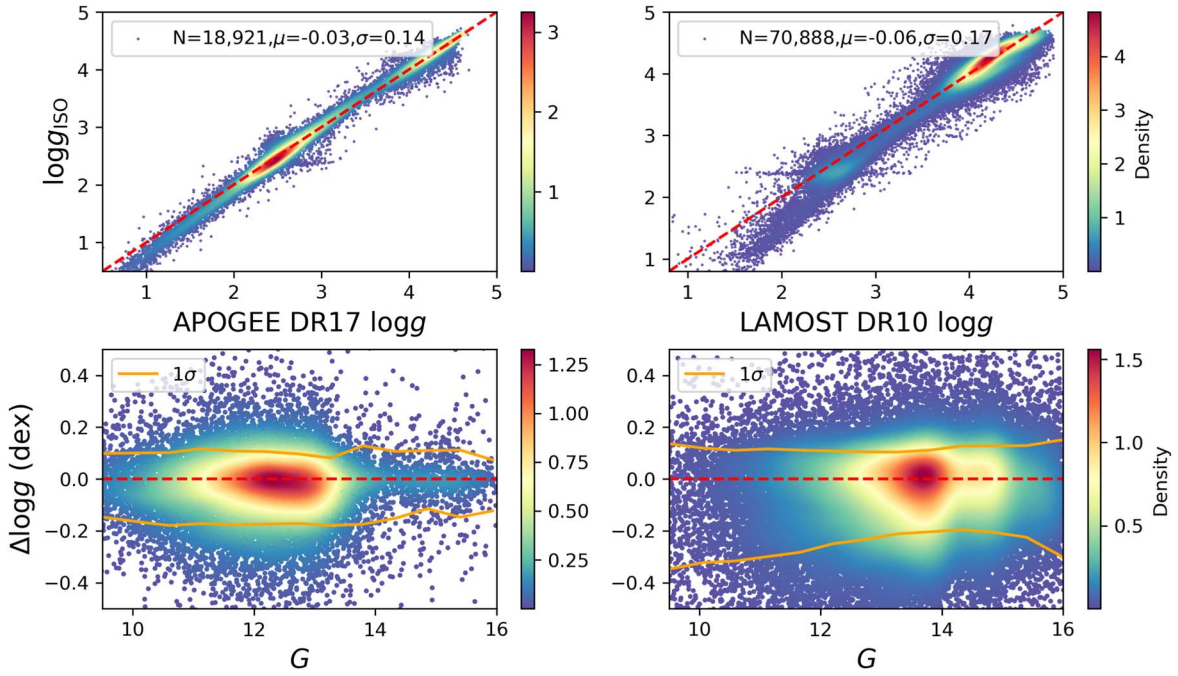

Figure 13. Comparison of log g obtained by the isochrone-fitting method with APOGEE DR17 (left panels) and LAMOST DR10 (right panels). The red dashed lines in the top panels are the one-to-one lines. The numbers of stars, mean offset, and dispersion are provided in the upper left corner of each panel in the top row. The bottom panels show the residuals in the sense of $\log g_{\text{isochrone fitting}} - \log g_{\text{APOGEE/LAMOST}}$, as a function of G magnitude. The red dashed lines in the bottom panels represent the zero level. The golden lines in the bottom panels represents the 1σ scatter. The color bar to the right of each panel codes the number density of stars in the panel.

There remains the problem that the theoretical metallicities given by PARSEC are in the form of [M/H], but the observed metallicities are in the form of [Fe/H]. We transformed the metallicities measured by [Fe/H] to [M/H] using Equation (6) from M. Salaris & S. Cassisi (2005):

$$[\mathrm{M/H}] = [\mathrm{Fe/H}] + \log(0.694 + 10^{[\alpha/\mathrm{Fe}]} + 0.306). \quad (4)$$

For $[\alpha/\mathrm{Fe}]$ in this relation, we fitted the $[\alpha/\mathrm{Fe}]$–[Fe/H] relation from the APOGEE $[\alpha/\mathrm{H}]$ and [Fe/H]. The fitting relation is a sixth-order polynomial; the parameters for this polynomial are listed in Table 2.

For the Bayesian estimation method, there are three parameters that decide stellar evolution: age τ, mass m, and metallicity Z. Thus, the posterior probability distribution function of the stellar parameters can be described as

$$f(\tau, M, Z) \propto f_0(\tau, M, Z)\mathcal{L}(\tau, M, Z), \quad (5)$$

where f_0 is the prior distribution of the parameters. In this work, we assumed that age and metallicity [M/H] follow a uniform distribution. For the mass, we assumed that it follows a power-law distribution given by E. E. Salpeter (1955):

$$f_0(M) \propto M^{-2.35}. \quad (6)$$

The prior distributions are independent of each other. $\mathcal{L}$ is the likelihood function of the parameters, which can be described as

$$\mathcal{L}(\tau, M, Z) = \prod_{i=1}^{n}\left(\frac{1}{\sqrt{2\pi}\,\sigma_i}\right) \times e^{-\frac{\chi^2}{2}}. \quad (7)$$

Here χ^2 is defined as

$$\chi^2 = \sum_{i=1}^{n}\left(\frac{O_i - T_i(\tau, M, Z)}{\sigma_i}\right)^2, \quad (8)$$

where O represents observational parameters, including the G-band absolute magnitude, intrinsic $(\mathrm{BP} - \mathrm{RP})_0$ color, and metallicity [M/H]. T are the theoretical values of those parameters given by the isochrone model under a specific set of parameters for τ, M, and Z.

With this procedure we can obtain the posterior probability distribution function (pdf), denoted as $\mathcal{L}(P|\tau, M, Z)$, for the parameter of interest. The parameters to be determined include stellar mass, age, surface gravity, and radius. For each parameter, we then calculate the pdf for each star using our Bayesian approach. The final estimate of each parameter for a given star is taken as the median of the resulting posterior pdf, with its uncertainty defined as half the difference between the 84th and 16th percentile values of the posterior pdf. The estimated physical parameters are then compared with independent measurements to assess their accuracy.

5.2. Comparison with APOGEE and LAMOST

The resulting log g values are compared with those from APOGEE DR17 and LAMOST DR10. As shown in Figure 13, the values from isochrone fitting are consistent with the spectroscopic measurements. The mean offsets are only −0.03 dex (isochrone fitting minus APOGEE) and −0.06 dex (isochrone fitting minus LAMOST), with small scatters of 0.14 and 0.17 dex, respectively. These comparisons indicate that our log g estimates from isochrone fitting are more accurate than those derived from stellar colors, as described above.

5.3. Comparison with SD18

To validate our age and mass estimates, we crossmatched our results with those from J. L. Sanders & P. Das (2018, hereafter SD18), which provides a catalog of stellar ages and

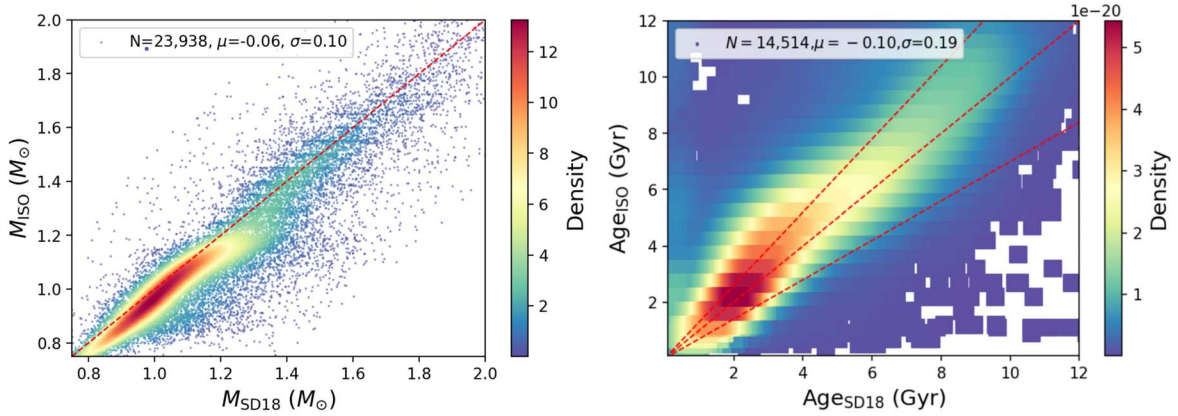

Figure 14. Comparisons of stellar mass (left panel) and age (right panel) estimates between this work and SD18 for, respectively, nearly 24,000 main-sequence stars and 14,000 main-sequence turnoff stars in common. The red dashed ine in the left panel is the one-to-one line. In the right panel, the red dashed lines indicate $Age_{ISO} = 1.3Age_{SD18}$ and $Age_{ISO} = 0.7Age_{SD18}$. The numbers of stars, mean offset, and dispersion are provided in the upper right corner of each panel. The color bar to the right of each panel codes the density number of stars in the panel.

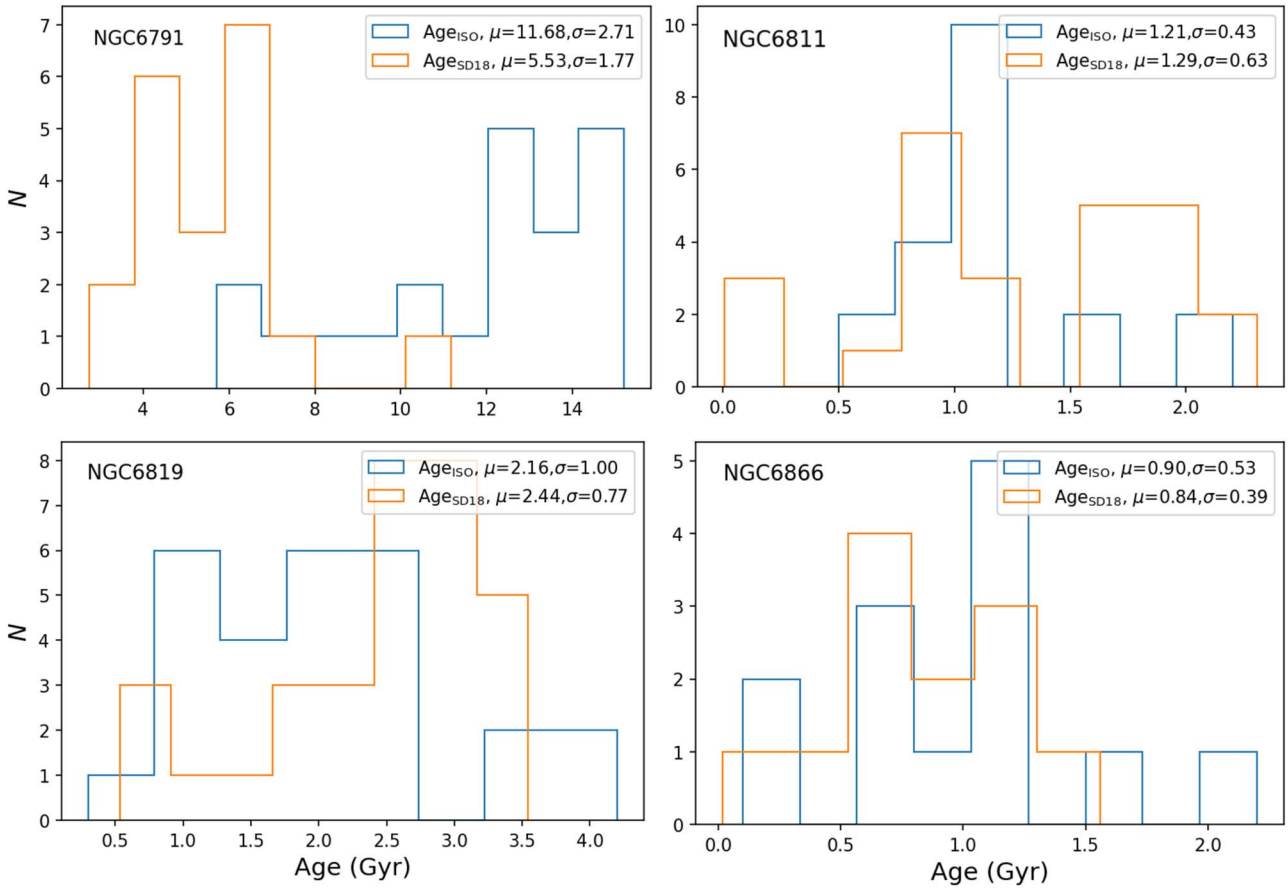

Figure 15. Age distributions for member stars of the four open clusters (NGC 6791, NGC 6811, NGC 6819, and NGC 6866) in the Kepler field. The blue lines represent the ages derived in this work, while the orange lines indicate the ages from SD18. The mean and dispersion of these distributions are marked in the upper right corner of each panel.

masses for approximately 3 million stars, derived from spectroscopic data from existing surveys combined with Gaia parallax measurements.

First, the stellar masses are compared with those from SD18 in Figure 14. Overall, the consistency is very good, with a mean offset of $-0.06\ M_\odot$ (our values minus those of SD18) and a scatter of $0.10\ M_\odot$. Note that giant stars are excluded from this comparison, as their mass estimates are highly sensitive to the uncertain parameter of mass loss, for which we adopted a constant value of $\eta_{\rm Reimers} = 0.2$, following the recommendation in PARSEC. We will later assess the masses of giant stars using asteroseismic estimates. Second, we compare our stellar ages with those from SD18, as shown in Figure 14. Only turnoff stars are included in this comparison, as their ages can be reliably constrained through isochrone fitting. The relative age ratio $(\tau_{\rm ISO} - \tau_{\rm SD18})/(\tau_{\rm ISO})$ shows a

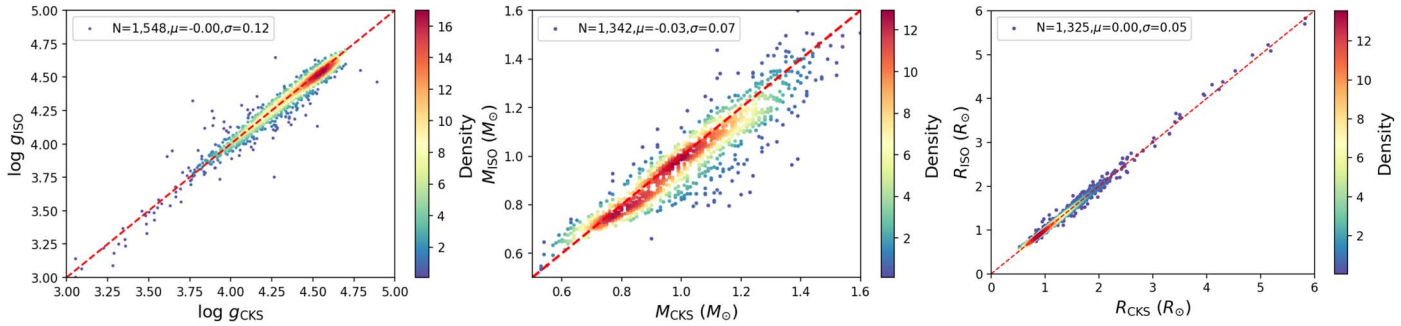

Figure 16. Comparisons of surface gravity (left panel), mass (middle panel), and radius (right panel) estimates between this work and CKS. The numbers of stars, mean offset (this work minus CKS), and scatter are marked in the upper left corner of each panel. The red dashed lines are one-to-one lines. The color bar to the right of each panel codes the number density of stars in the panel.

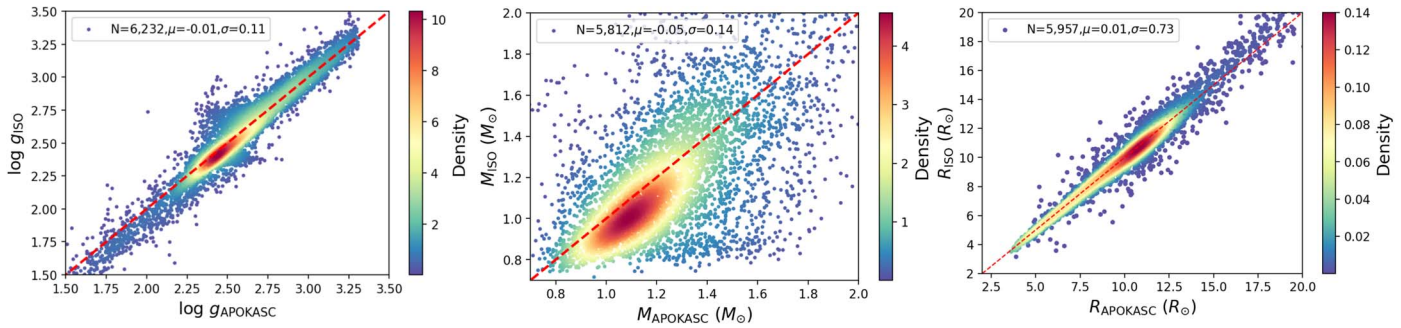

Figure 17. Similar to Figure 16, but for comparison with APOKASC.

mean offset of +10%, with a dispersion around 19%. To further evaluate the precision of isochrone-derived ages, we selected members of open clusters using the method described in Section 3. Figure 15 shows the age distributions for member stars of four open clusters in the Kepler field. The median values of these distributions are close to those reported by other independent studies (L. N. Brewer et al. 2016; E. L. Sandquist et al. 2016; D. Bossini et al. 2019; K. Brogaard et al. 2021; see Table A1).

5.4. Comparison with CKS

As previously described, CKS is a high-resolution spectroscopic survey designed to determine the properties of exoplanets and their host stars in the Kepler field. Observations conducted with the Keck telescope have provided atmospheric parameters and other characteristics for approximately 1700 exoplanet-host stars. Using the Keck spectra, E. A. Petigura et al. (2017, 2018) derived the stellar atmospheric parameters (effective temperature, surface gravity, and metallicity) for the exoplanet-host stars. Based on these parameters, J. A. Johnson et al. (2017) further determined the masses and radii of these stars.

As shown in Figure 16, the isochrone-derived log g is in excellent agreement with that of CKS, with no offset and a minimal scatter of 0.12 dex. Both stellar mass and radius from isochrone fitting are also in very close agreement with CKS results. The offsets are negligible, with no offset for radius and only $-0.03\ M_\odot$ (our values minus those of CKS) for mass. The scatter is just 0.07 $M_\odot$ for mass and 0.05 $R_\odot$ for radius.

5.5. Comparison with APOKASC

Asteroseismology is an important technique in the field of stellar parameter measurement, as it enables precise estimates of mass, radius, and surface gravity. Here we compare our results with those from the Apache Point Observatory Galactic Evolution Experiment and the Kepler Asteroseismic Science Consortium (APOKASC; M. H. Pinsonneault et al. 2014, 2018). The APOKASC catalog provides stellar parameters derived by combining asteroseismic data (such as frequency spacing $\Delta\mu$ and maximum oscillation frequency μ_{max}, from which mass and radius can be estimated) from the Kepler Asteroseismic Science Consortium (KASC) with spectroscopic data (such as T_{eff}, [Fe/H]) from APOGEE.

We compared our isochrone-derived log g, mass, and radius with those from APOKASC. As shown in Figure 17, all parameters estimated from isochrone fitting exhibit good agreement with APOKASC results. For log g, the mean offset is only -0.01 dex (our result minus APOKASC), with a dispersion of 0.11 dex. For stellar radius, there is an offset of 0.01 $R_\odot$, and the scatter is only 0.73 $R_\odot$. For stellar mass, a slight offset of $-0.05 M_\odot$ (our result minus APOKASC) is observed, with a moderate scatter of 0.14 $M_\odot$. This offset and dispersion are at least partly due to uncertainties in the mass-loss parameter for red giant stars.

6. Final Sample and Notes for Their Use

Using the methods described above, we have obtained physical parameter estimates for around 190,000 KIC stars. However, around 10,000 KIC stars still lack these estimates. An examination of the H-R diagram (see Figure 18) reveals that most of the stars without parameter estimates are cool dwarfs

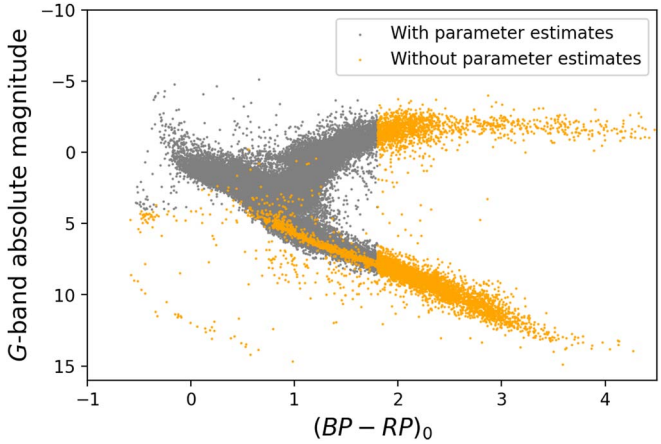

Figure 18. Distribution of KIC stars (orange circles) without reliable parameter estimates on the color–*G*-band absolute magnitude diagram. The background gray circles represent stars with well-determined atmospheric and physical parameters.

Table 3
Sample Content

Parameter Type	Method	Number of A, F, G, K Stars	Number of M Stars	Total
Photometric [Fe/H]	KIS *U*-band photometry	179,133	⋯	179,133
	Synthesized *v*, *b*, *y* photometry	189,727	5252	194,979
	One of the above methods	190,226	5252	195,478
Photometric $T_{\rm eff}$	$T_{\rm eff}$–[Fe/H]–color relation	189,727	5252	194,979
Photometric log *g*	log *g* –[Fe/H]–color relation	179,133	4285	183,418
Age, mass, and radius	Isochrone fitting	185,886	⋯	185,886

and giants with $(\mathrm{BP}-\mathrm{RP})_0 \geqslant 1.8$, as well as hot subdwarfs and white dwarfs. These stars were excluded from the training process owing to the challenges in obtaining reliable parameter estimates for them. Additionally, a small number of main-sequence and turnoff stars lack parameter estimates because they do not have Gaia XP spectra or KIS photometry observations.

6.1. Parameters of M-type Stars

To obtain parameters for as many KIC stars as possible, we trained the photometric parameter relations for M-type stars using a method similar to that described in Section 4. Recently, LAMOST DR10 released stellar atmospheric parameters for both M dwarf and giant stars using the LASPM pipeline (B. Du et al. 2021). We crossmatched our sample of cool stars with $(\mathrm{BP}-\mathrm{RP})_0 \geqslant 1.8$ against the LAMOST M dwarf and giant catalog, finding over 1500 stars (582 dwarfs and 981 giants). Using the same training methods described in Section 4, we derived relationships between atmospheric parameters and synthesized Strömgren photometry for both M dwarfs and giants. These relationships were then applied to over 5200 cool stars to estimate their missing atmospheric parameters. To assess the precision of our estimates, we crossmatched these stars with APOGEE DR17, finding around 100 M dwarfs and 1000 M giants in common. The comparisons indicate moderate offsets across all atmospheric parameters, with typical values around 0.10 dex for [M/H], 120 K for $T_{\rm eff}$, and 0.10 dex for log *g*. The dispersions are 0.20 dex for both log *g* and [M/H] and relatively low for $T_{\rm eff}$, at about 60 K. Due to the limited accuracy of the parameters (large offsets and dispersion), we do not proceed with isochrone-based estimates of physical parameters derived from these stellar atmospheric parameters.

6.2. Data Access

In the final tables, we present data from two separate stellar catalogs: one for AFGK stars and another for M-type stars. A detailed description of the catalogs is provided in Table C1. The updated KIC parameter catalogs are publicly available on Zenodo at doi:10.5281/zenodo.14546166.

6.3. Notes for Using Data

If one wishes to use the data from these tables, please take note of the following points:

1. *Parameters of M-type Stars.* Due to the relatively small size of the training set and limited data available for comparison and verification, the reliability of M-type star parameters is lower compared to that of AFGK stars. Caution is advised when using these values for further analysis.
2. *Stellar Classification.* The classification of stellar types on the H-R diagram in this paper is based on empirical methods. Some mixtures may occur at the classification boundaries, particularly between main-sequence stars and binary stars.
3. *Isochrone Fitting.* While the isochrone-fitting method provides reliable mass and age estimates for turnoff stars and subgiant stars, there is greater uncertainty for other stellar types. These uncertainties should be carefully taken into account during analysis.
4. *Surface Gravity.* In this work, stellar surface gravity was estimated using both stellar colors and isochrone fitting. Based on various checks, the accuracy of the isochrone-fitting method is significantly better than that derived from stellar colors. Therefore, when surface gravity

estimates are available from both methods, we recommend using the values obtained from isochrone fitting.

7. Summary

In this work, we have made three main improvements to the KIC: (1) established a high-precision 3D extinction map of the Kepler field, (2) obtained atmospheric parameter estimates for 97% of KIC stars using photometric data from KIS and Gaia XP, and (3) derived stellar mass, radius, surface gravity, and age estimates for these KIC stars based on their atmospheric parameters and stellar evolution models. Details of these improvements are outlined below.

1. First, we determined the extinction for stars in the Kepler field using the SP method and constructed a 3D extinction map for this region. By analyzing members of four well-known open clusters within the Kepler field, we found that this new 3D extinction map provides more accurate reddening values than those from the commonly used map by G. M. Green et al. (2019).
2. By training a relationship between the photometric colors from KIS DR2, the ultra–wide-band photometric colors from Gaia DR3, the photometric colors synthetically generated from the Gaia XP spectra, and the spectral stellar parameters from LAMOST DR10, we obtained atmospheric parameter estimates for about 195,000 stars, accounting for 97% of the total number of the KIC stars. We achieved uncertainties of 0.12 dex on [Fe/H], 100 K on $T_{\rm eff}$, and 0.2 dex on log g.
3. Using the PARSEC stellar evolution model, we estimated the masses, radii, surface gravities, and ages of KIC stars based on their atmospheric parameters and photometric data. We then compared our mass and age estimates with values from the literature, especially stars with mass, radius, and surface gravity measurements from asteroseismology data. These comparisons indicate that our estimates achieve precisions of 0.07 $M_{\odot}$ in mass, 0.05 $R_{\odot}$ in radius, and 0.12 dex in surface gravity for dwarf stars and 0.14 $M_{\odot}$ in mass, 0.73 $R_{\odot}$ in radius, and 0.11 dex in surface gravity for giant stars.

We summarize the methodology for each parameter estimate in Table 3. These results are expected to be valuable for future research on exoplanet-host stars, exoplanet habitability, and asteroseismology studies.

Acknowledgments

Y.H. acknowledges the support from the National Key R&D Program of China (grant No. 2019YFA0405503) and the National Science Foundation of China (NSFC grant No. 12422303). T.C.B. acknowledges partial support for this work from grant PHY 14-30152; Physics Frontier Center/JINA Center for the Evolution of the Elements (JINA-CEE); and OISE-1927130: The International Research Network for Nuclear Astrophysics (IReNA), awarded by the US National Science Foundation. K.X. acknowledges the support of the NSFC grant No. 12403024, the Postdoctoral Fellowship Program of CPSF under grant No. GZB20240731, the Young Data Scientist Project of the National Astronomical Data Center, and the China Postdoctoral Science Foundation No. 2023M743447.

This work presents results from the European Space Agency's space mission Gaia (https://www.cosmos.esa.int/gaia). Gaia data are processed by the Gaia Data Processing and Analysis Consortium (https://www.cosmos.esa.int/web/gaia/dpac/consortium), which is funded by national institutions, in particular the institutions participating in the Gaia Multilateral Agreement.

Software: Astropy (Astropy Collaboration et al. 2013, 2018, 2022), Dustmaps (G. M. Green 2018), Matplotlib (J. D. Hunter 2007), multiprocessing (M. M. McKerns et al. 2012) NumPy (C. R. Harris et al. 2020), pandas (The pandas development team 2024), Scikit-learn (F. Pedregosa et al. 2011), SciPy (P. Virtanen et al. 2020), Topcat (M. B. Taylor 2005).

Appendix A
Extinction Map Comparison

Here we summarize the adopted parameters for the four open clusters in the Kepler field (Table A1), compare the reddening values obtained based on our 3D extinction map of the Kepler field with the values of reddening adopted by G. M. Green et al. (2019; see Figure A1), and compare the reddening values from our 3D extinction map for member stars in the four open clusters in the Kepler field with those adopted by G. M. Green et al. (2019; see Figure A2).

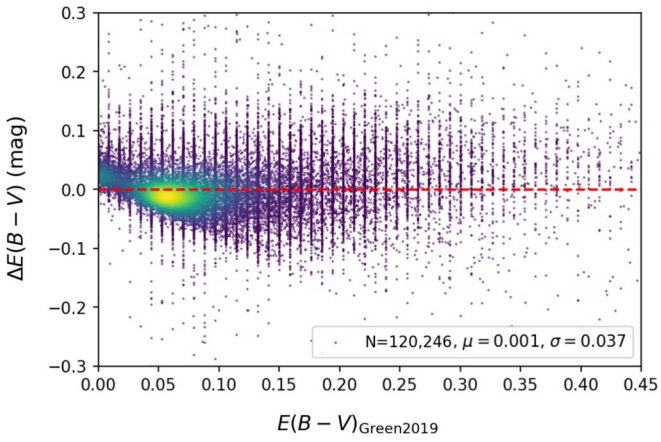

Figure A1. Comparison of reddening values between those derived using the SP method in this work and those from the 3D extinction map of G. M. Green et al. (2019). $\Delta E(B-V)$ represents the difference between the reddening values obtained from the SP method and those from the 3D extinction map of G. M. Green et al. (2019). The red dashed line represents the zero level. The mean and scatter of this difference are indicated in the lower right corner.

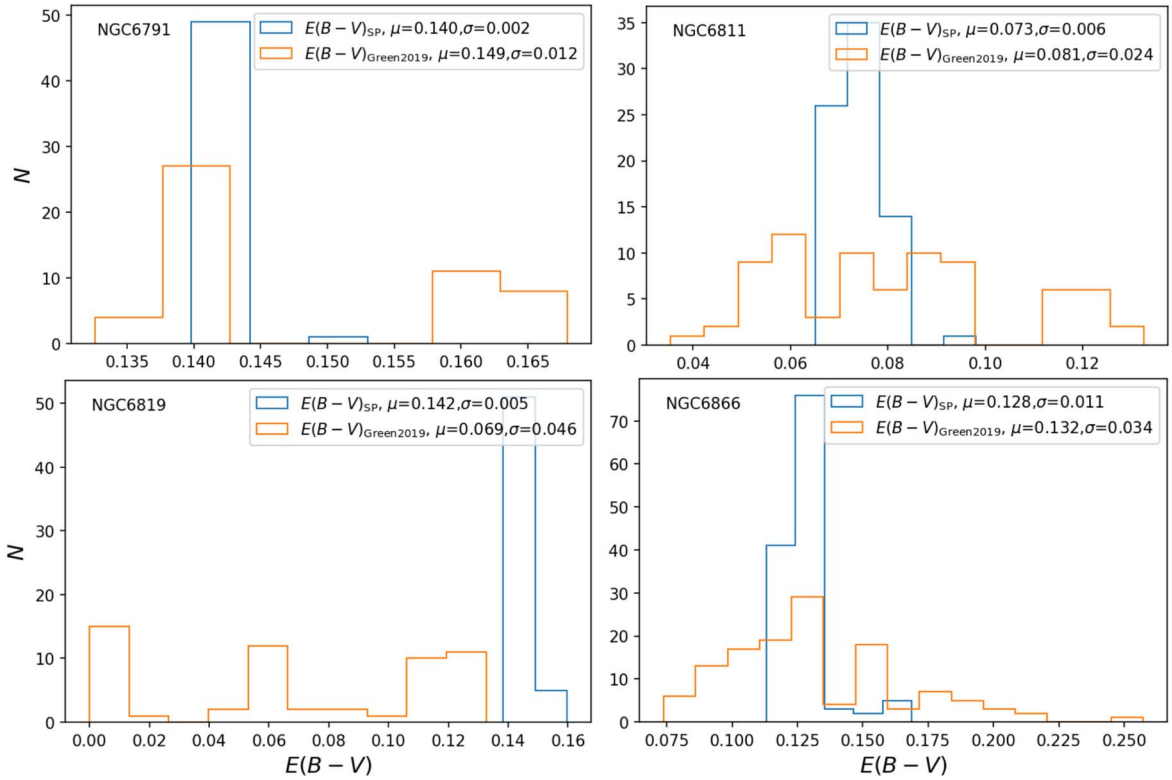

Figure A2. Reddening values for member stars of four open clusters (NGC 6791, NGC 6811, NGC 6819, and NGC 6866) in the Kepler field. The blue lines represent $E(B-V)$ given by our 3D extinction map, while the orange lines indicate the $E(B-V)$ from the map of G. M. Green et al. (2019). The mean and dispersion of these distributions are marked in the upper right corner of each panel.

Table A1
Parameters of Open Clusters in the Kepler Field

NGC Number	Distance[a] (kpc)	R.A.[a] (deg)	Decl.[a] (deg)	$PM^{a}_{R.A.}$ (mas yr^{-1})	$PM^{a}_{decl.}$ (mas yr^{-1})	$E(B-V)$ (mag)	Age (Gyr)
NGC 6791	4.2	290.22	37.77	−0.42	−2.28	0.10[a]/0.14[b]	8.30[c]/11.7[b]
NGC 6811	1.1	294.34	46.36	−3.35	−8.80	0.074[d]/0.072[b]	1.05[e]/1.21[b]
NGC 6819	2.5	295.32	40.19	−2.90	−3.87	0.16[f]/0.14[b]	2.38[g]/2.16[b]
NGC 6866	1.4	300.98	44.16	−1.37	−5.76	0.13[h]/0.13[b]	0.78[h]/0.90[b]

Notes.
[a] E. L. Hunt & S. Reffert (2023).
[b] This work.
[c] K. Brogaard et al. (2021).
[d] K. Janes et al. (2013).
[e] E. L. Sandquist et al. (2016).
[f] B. J. Anthony-Twarog et al. (2014).
[g] L. N. Brewer et al. (2016).
[h] D. Bossini et al. (2019).

Appendix B
Supplementary Metallicity Comparison Test

Here we provide comparisons of the photometric metallicity estimates from the KIS photometry for turnoff stars and binary stars with those from APOGEE DR17 (Figure B1) and comparisons of the photometric metallicity estimates from Strömgren photometry synthesized from the Gaia XP spectra for turnoff stars and binary stars with those from APOGEE DR17 (Figure B2).

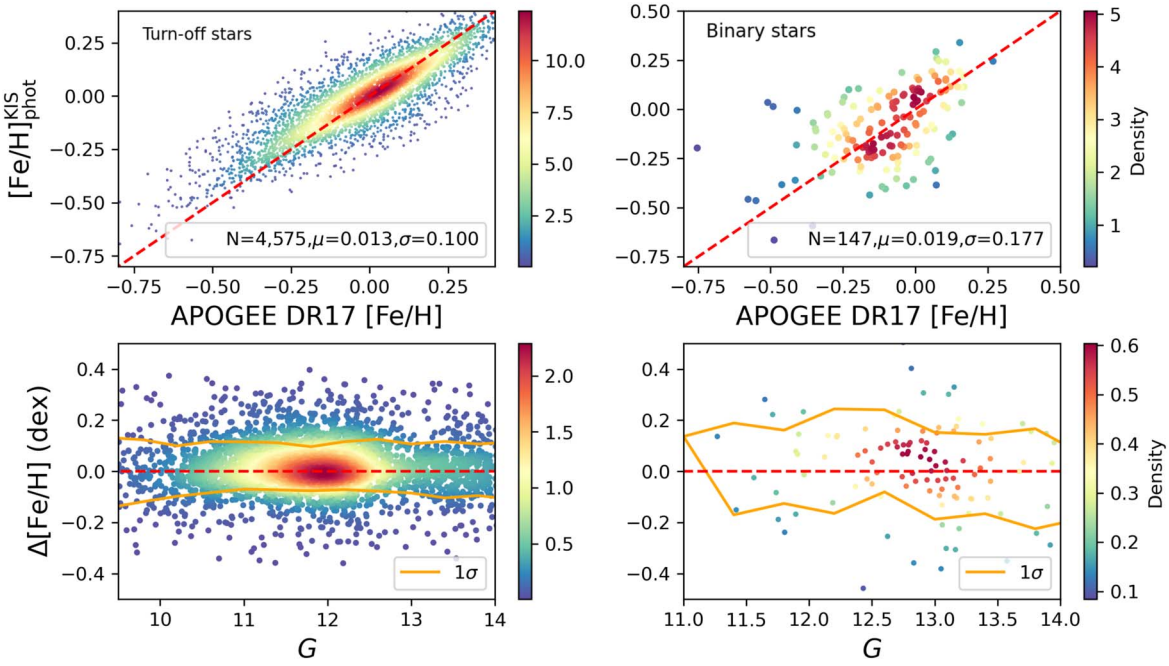

Figure B1. Comparisons of photometric metallicity estimates from the KIS photometry with those from the APOGEE DR17 for the turnoff stars (left panels) and binary stars (right panels). The red dashed lines in the top panels are the one-to-one lines. The numbers of stars, mean offset, and scatter are provided in the lower right corner of each panel. The bottom panels are the residuals of metallicity differences ($[Fe/H]_{phot}$–$[Fe/H]_{APOGEE}$) as a function of Gaia G magnitude. The red dashed lines in the bottom panels represent the zero level. The gold lines in the bottom panels represent the 1σ scatter. The color bar to the right of each panel codes the number density of stars in the panel.

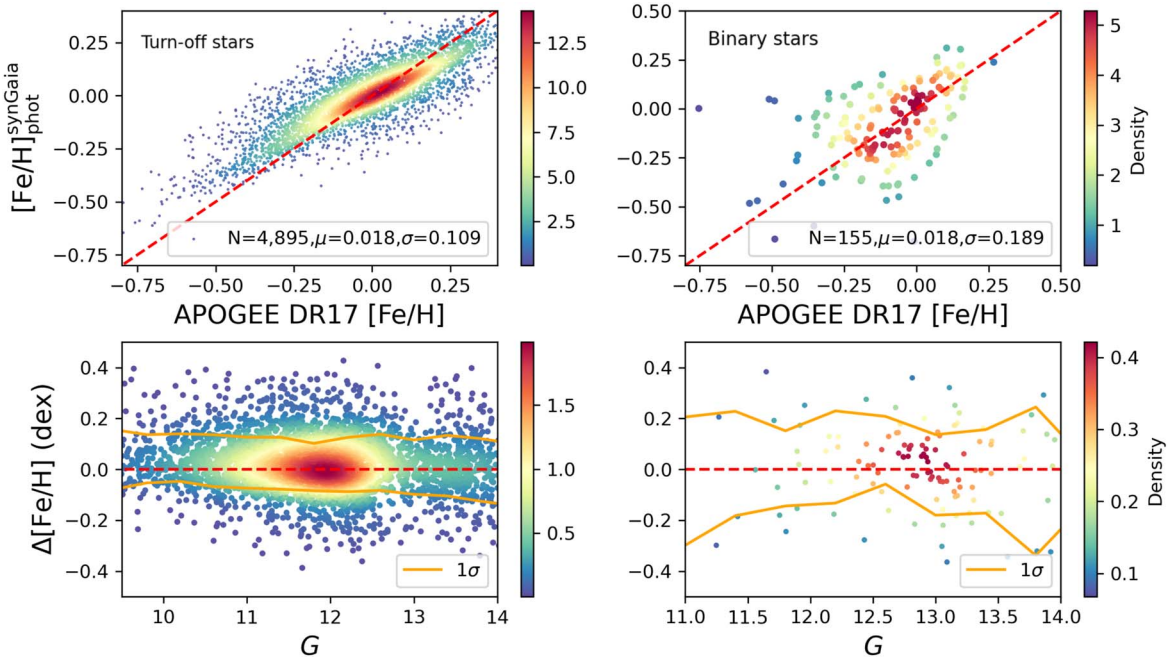

Figure B2. Similar to Figure B1, but for photometric metallicity estimates from the Strömgren photometry synthesized from the Gaia XP spectra.

Appendix C
Catalog Description

In Table C1 we provide a detailed listing of the contents of our final catalog, including the input quantities and their sources, as well as the derived quantities and estimates of stellar atmospheric parameters from LAMOST DR10 and APOGEE DR17. The updated KIC parameter catalogs will be publicly available on Zenodo at doi:10.5281/zenodo.14546166.

Table C1
Catalog Description

Column Name	Description
kepid	ID of the KIC star
SourceID	Source ID of Gaia DR3
degree_ra	R.A. of KIC star
degree_dec	Decl. of KIC star
G	G-band photometry from Gaia DR3
G_err	Uncertainty of G-band photometry from Gaia DR3
BP	BP-band photometry from Gaia DR3
BP_err	Uncertainty of BP-band photometry from Gaia DR3
RP	RP-band photometry from Gaia DR3
RP_err	Uncertainty of RP-band photometry from Gaia DR3
BP − RP	BP − RP color from Gaia DR3
v	v-band photometry synthesized from Gaia DR3 XP spectra
v_err	Uncertainty of v-band photometry synthesized from Gaia DR3 XP spectra
b	b-band photometry synthesized from Gaia DR3 XP spectra
b_err	Uncertainty of b-band photometry synthesized from Gaia DR3 XP spectra
y	y-band photometry synthesized from Gaia DR3 XP spectra
y_err	Uncertainty of y-band photometry synthesized from Gaia DR3 XP spectra
U	U-band photometry from KIS DR2
U_err	Uncertainty of U-band photometry from KIS DR2
E(BP − RP)	BP − RP excess from our 3D extinction map
FeH_KIS_PHOT/MH_KIS_PHOT[a]	[Fe/H]/[M/H] from KIS colors
FeH_KIS_PHOT_err/MH_KIS_PHOT_err[a]	Uncertainty of [Fe/H]/[M/H] from KIS colors
FeH_GaiaSyn_PHOT/MH_GaiaSyn_PHOT[a]	[Fe/H]/[M/H] from Gaia-synthesized colors
FeH_GaiaSyn_PHOT_err/MH_GaiaSyn_PHOT_err[a]	Uncertainty of [Fe/H]/[M/H] from Gaia-synthesized colors
$T_{\rm eff}$_PHOT	Photometric effective temperature
$T_{\rm eff}$_PHOT_err	Photometric uncertainty of effective temperature
log g_PHOT	Photometric surface gravity
log g_PHOT_err	Photometric uncertainty of surface gravity
Age_ISO[b]	Age by isochrone-fitting method
Age_ISO_low[b]	16th percentile of age posterior by isochrone-fitting method
Age_ISO_up[b]	84th percentile of age posterior by isochrone-fitting method
M_ISO[b]	Mass by isochrone-fitting method
M_ISO_err[b]	Uncertainty of mass fitted by isochrone-fitting method
log g_ISO[b]	Surface gravity by isochrone-fitting method
log g_ISO_err[b]	Uncertainty of surface gravity by isochrone-fitting method
$T_{\rm eff}$_ISO[b]	Effective temperature by isochrone-fitting method
$T_{\rm eff}$_ISO_err[b]	Uncertainty of effective temperature by isochrone-fitting method
log L_ISO[b]	Luminosity by isochrone-fitting method
log L_ISO_err[b]	Uncertainty of luminosity by isochrone-fitting method
R_ISO[b]	Radius by isochrone-fitting method
R_ISO_err[b]	Uncertainty of radius fitted by isochrone-fitting method
FeH_LAMOST/MH_LAMOST[c]	[Fe/H]/[M/H] from LAMOST DR10
FeH_LAMOST_err/MH_LAMOST_err[c]	Uncertainty of [Fe/H]/[M/H] from LAMOST DR10
$T_{\rm eff}$_LAMOST	Effective temperature from LAMOST DR10
$T_{\rm eff}$_LAMOST_err	Uncertainty of effective temperature from LAMOST DR10
log g_LAMOST	Surface gravity from LAMOST DR10
log g_LAMOST_err	Uncertainty of surface gravity from LAMOST DR10
FeH_APOGEE	[Fe/H] from APOGEE DR17
FeH_APOGEE_err	Uncertainty of [Fe/H] from APOGEE DR17
$T_{\rm eff}$_APOGEE	Effective temperature from APOGEE DR17
$T_{\rm eff}$_APOGEE_err	Uncertainty of effective temperature from APOGEE DR17
log g_APOGEE	Surface gravity from APOGEE DR17
log g_APOGEE_err	Uncertainty of surface gravity from APOGEE DR17
MH_APOGEE	[M/H] from APOGEE DR17
MH_APOGEE_err	Uncertainty of [M/H] from APOGEE DR17
pmra	Proper motion in R.A. direction from Gaia DR3
pmra_err	Uncertainty of proper motion in R.A. direction from Gaia DR3
pmdec	Proper motion in decl. direction from Gaia DR3
pmdec_err	Uncertainty of proper motion in decl. direction from Gaia DR3
rgeo	Geometric distance from C. A. L. Bailer-Jones et al. (2021)
rgeo_low	16th percentile of the geometric distance posterior from C. A. L. Bailer-Jones et al. (2021)
rgeo_up	84th percentile of the geometric distance posterior from C. A. L. Bailer-Jones et al. (2021)
rpgeo	Photogeometric distance from C. A. L. Bailer-Jones et al. (2021)

Table C1
(Continued)

Column Name	Description
rpgeo_low	16th percentile of the photogeometric distance posterior from C. A. L. Bailer-Jones et al. (2021)
rpgeo_up	84th percentile of the photogeometric distance posterior from C. A. L. Bailer-Jones et al. (2021)
StarType	Type of KIC star, including TO (turnoff), giant, (MS) main sequence, binary, HS (hot star), gM (M-type giant), and dM (M-type dwarf)

Notes.
[a] [Fe/H] for A-, F-, G-, and K-type stars and [M/H] for M-type dwarfs.
[b] Only for A-, F-, G-, and K-type stars.
[c] [Fe/H] for A-, F-, G-, and K-type stars and [M/H] for M-type stars.

ORCID iDs

Bowen Zhang https://orcid.org/0009-0008-7479-0742
Yang Huang https://orcid.org/0000-0003-3250-2876
Timothy C. Beers https://orcid.org/0000-0003-4573-6233
Kai Xiao https://orcid.org/0000-0001-8424-1079
Jifeng Liu https://orcid.org/0000-0002-2874-2706
Henggeng Han https://orcid.org/0000-0003-3474-5118
Zhirui Li https://orcid.org/0000-0002-7598-9250
Chuanjie Zheng https://orcid.org/0009-0006-7556-8401
Yongkang Sun https://orcid.org/0000-0002-3935-2666
Ruifeng Shi https://orcid.org/0009-0000-6932-7894
Hongrui Gu https://orcid.org/0009-0007-5610-6495

References

Ahn, C. P., Alexandroff, R., Allende Prieto, C., et al. 2012, ApJS, 203, 21
Anthony-Twarog, B. J., Deliyannis, C. P., & Twarog, B. A. 2014, AJ, 148, 51
Astropy Collaboration, Price-Whelan, A. M., Lim, P. L., et al. 2022, ApJ, 935, 167
Astropy Collaboration, Price-Whelan, A. M., Sipőcz, B. M., et al. 2018, AJ, 156, 123
Astropy Collaboration, Robitaille, T. P., Tollerud, E. J., et al. 2013, A&A, 558, A33
Bailer-Jones, C. A. L., Rybizki, J., Fouesneau, M., Demleitner, M., & Andrae, R. 2021, AJ, 161, 147
Berger, T. A., Huber, D., van Saders, J. L., et al. 2020, AJ, 159, 280
Boley, K. M., Christiansen, J. L., Zink, J., et al. 2024, AJ, 168, 128
Borucki, W. J. 2016, RPPh, 79, 036901
Borucki, W. J., Koch, D., Basri, G., et al. 2010, Sci, 327, 977
Bossini, D., Vallenari, A., Bragaglia, A., et al. 2019, A&A, 623, A108
Breiman, L. 2001, Mach. Learn., 45, 5
Bressan, A., Marigo, P., Girardi, L., et al. 2012, MNRAS, 427, 127
Brewer, L. N., Sandquist, E. L., Mathieu, R. D., et al. 2016, AJ, 151, 66
Brogaard, K., Grundahl, F., Sandquist, E. L., et al. 2021, A&A, 649, A178
Brown, T. M., Latham, D. W., Everett, M. E., & Esquerdo, G. A. 2011, AJ, 142, 112
Burn, R., Mordasini, C., Mishra, L., et al. 2024, NatAs, 8, 463
Carrasco, J. M., Weiler, M., Jordi, C., et al. 2021, A&A, 652, A86
Chaplin, W. J., Basu, S., Huber, D., et al. 2014, ApJS, 210, 1
Chiti, A., Frebel, A., Mardini, M. K., et al. 2021, ApJS, 254, 31
De Angeli, F., Weiler, M., Montegriffo, P., et al. 2023, A&A, 674, A2
De Cat, P., Fu, J. N., Ren, A. B., et al. 2015, ApJS, 220, 19
Dong, S., Zheng, Z., Zhu, Z., et al. 2014, ApJL, 789, L3
Du, B., Luo, A. L., Zhang, S., et al. 2021, RAA, 21, 202
Fan, Z., Zhao, G., Wang, W., et al. 2023, ApJS, 268, 9
Fu, J., Zong, W., & Wang, H. 2022, SSPMA, 52, 289502
Fu, J.-N., Cat, P. D., Zong, W., et al. 2020, RAA, 20, 167
Gaia Collaboration, Brown, A. G. A., Vallenari, A., et al. 2021a, A&A, 649, A1
Gaia Collaboration, Brown, A. G. A., Vallenari, A., et al. 2021b, A&A, 650, C3
Gaia Collaboration, Vallenari, A., Brown, A. G. A., et al. 2023, A&A, 674, A1
Garcìa Pérez, A. E., Allende Prieto, C., Holtzman, J. A., et al. 2016, AJ, 151, 144
Gilliland, R. L., Brown, T. M., Christensen-Dalsgaard, J., et al. 2010, PASP, 122, 131
Gonzalez, G. 1997, MNRAS, 285, 403
Green, G. M. 2018, JOSS, 3, 695
Green, G. M., Schlafly, E., Zucker, C., Speagle, J. S., & Finkbeiner, D. 2019, ApJ, 887, 93
Greiss, S., Steeghs, D., Gänsicke, B. T., et al. 2012a, AJ, 144, 24
Greiss, S., Steeghs, D., Gänsicke, B. T., et al. 2012b, arXiv:1212.3613
Hardegree-Ullman, K. K., Zink, J. K., Christiansen, J. L., et al. 2020, ApJS, 247, 28
Harris, C. R., Millman, K. J., van der Walt, S. J., et al. 2020, Natur, 585, 357
Howell, S. B., Sobeck, C., Haas, M., et al. 2014, PASP, 126, 398
Huang, Y., Beers, T. C., Wolf, C., et al. 2022, ApJ, 925, 164
Huang, Y., Beers, T. C., Xiao, K., et al. 2024, ApJ, 974, 192
Huang, Y., Beers, T. C., Yuan, H., et al. 2023, ApJ, 957, 65
Huang, Y., Chen, B. Q., Yuan, H. B., et al. 2019, ApJS, 243, 7
Huber, D., Silva Aguirre, V., Matthews, J. M., et al. 2014, ApJS, 211, 2
Huber, D., & Zwintz, K. 2020, Stars and their Variability Observed from Space, ed. C. Neiner et al., 457
Hunt, E. L., & Reffert, S. 2023, A&A, 673, A114
Hunter, J. D. 2007, CSE, 9, 90
Janes, K., Barnes, S. A., Meibom, S., & Hoq, S. 2013, AJ, 145, 7
Johnson, J. A., Aller, K. M., Howard, A. W., & Crepp, J. R. 2010, PASP, 122, 905
Johnson, J. A., Petigura, E. A., Fulton, B. J., et al. 2017, AJ, 154, 108
Jørgensen, B. R., & Lindegren, L. 2005, A&A, 436, 127
Karoff, C., Metcalfe, T. S., Santos, Â. R. G., et al. 2018, ApJ, 852, 46
Li, X.-Y., Huang, Y., Liu, G.-C., Beers, T. C., & Zhang, H.-W. 2023, ApJ, 944, 88
Loaiza-Tacuri, V., Cunha, K., Smith, V. V., et al. 2024, ApJ, 970, 53
Lopez, E. D., & Fortney, J. J. 2013, ApJ, 776, 2
Masuda, K. 2022, ApJ, 937, 94
Mathur, S., Huber, D., Batalha, N. M., et al. 2017, ApJS, 229, 30
McKerns, M. M., Strand, L., Sullivan, T., Fang, A., & Aivazis, M. A. G. 2012, arXiv:1202.1056
McQuillan, A., Mazeh, T., & Aigrain, S. 2014, ApJS, 211, 24
Montegriffo, P., De Angeli, F., Andrae, R., et al. 2023, A&A, 674, A3
Owen, J. E., & Wu, Y. 2017, ApJ, 847, 29
Pedregosa, F., Varoquaux, G., Gramfort, A., et al. 2011, JMLR, 12, 2825
Petigura, E. A., Howard, A. W., Marcy, G. W., et al. 2017, AJ, 154, 107
Petigura, E. A., Marcy, G. W., Winn, J. N., et al. 2018, AJ, 155, 89
Pinsonneault, M., Elsworth, Y., Silva Aguirre, V., et al. 2018, AAS Meeting, 231, 450.13
Pinsonneault, M. H., Elsworth, Y., Epstein, C., et al. 2014, ApJS, 215, 19
Pinsonneault, M. H., Elsworth, Y. P., Tayar, J., et al. 2018, ApJS, 239, 32
Riello, M., De Angeli, F., Evans, D. W., et al. 2021, A&A, 649, A3
Rockosi, C. M., Lee, Y. S., Morrison, H. L., et al. 2022, ApJS, 259, 60
Ruz-Mieres, D., & zuzannakr, 2022 gaia-dpci/GaiaXPy: GaiaXPy v2.1.2, Zenodo, doi:10.5281/zenodo.6558515
Salaris, M., & Cassisi, S. 2005, Evolution of Stars and Stellar Populations (Chichester: John Wiley & Sons Ltd)
Salpeter, E. E. 1955, ApJ, 121, 161
Sanders, J. L., & Das, P. 2018, MNRAS, 481, 4093
Sandquist, E. L., Jessen-Hansen, J., Shetrone, M. D., et al. 2016, ApJ, 831, 11
Schlegel, D. J., Finkbeiner, D. P., & Davis, M. 1998, ApJ, 500, 525
See, V., Roquette, J., Amard, L., & Matt, S. 2023, MNRAS, 524, 5781
Shibayama, T., Maehara, H., Notsu, S., et al. 2013, ApJS, 209, 5
Stello, D., Huber, D., Bedding, T. R., et al. 2013, ApJL, 765, L41
Strömgren, B. 1963, QJRAS, 4, 8
Sun, Y., Yuan, H., & Chen, B. 2022, ApJS, 260, 17

Taylor, M. B. 2005, in ASP Conf. Ser. 347, Astronomical Data Analysis Software and Systems XIV, ed. P. Shopbell, M. Britton, & R. Ebert (San Francisco, CA: APS), 29
The pandas development team 2024, pandas-dev/pandas: Pandas, v2.2.1, Zenodo, doi:10.5281/zenodo.3509134
Tian, H.-J., El-Badry, K., Rix, H.-W., & Gould, A. 2020, ApJS, 246, 4
Tremonti, C. A., Heckman, T. M., Kauffmann, G., et al. 2004, ApJ, 613, 898
Virtanen, P., Gommers, R., Oliphant, T. E., et al. 2020, NatMe, 17, 261
Wang, S., & Chen, X. 2019, ApJ, 877, 116
Witzke, V., Reinhold, T., Shapiro, A. I., Krivova, N. A., & Solanki, S. K. 2020, A&A, 634, L9
Wu, Y., Du, B., Luo, A., Zhao, Y., & Yuan, H. 2014, in IAU Symp. 306, Statistical Challenges in 21st Century Cosmology, ed. A. Heavens, J.-L. Starck, & A. Krone-Martins (Cambridge: Cambridge Univ. Press), 340
Wu, Y., Luo, A. L., Li, H.-N., et al. 2011, RAA, 11, 924
Yanny, B., Rockosi, C., Newberg, H. J., et al. 2009, AJ, 137, 4377
Yu, J., Huber, D., Bedding, T. R., et al. 2016, MNRAS, 463, 1297
Yuan, H., Liu, X., Xiang, M., Huang, Y., & Chen, B. 2015a, ApJ, 799, 134
Yuan, H., Liu, X., Xiang, M., Huang, Y., & Chen, B. 2015b, ApJ, 803, 13
Yuan, H. B., Liu, X. W., & Xiang, M. S. 2013, MNRAS, 430, 2188
Yun, S., Lee, Y. S., Kim, Y. K., et al. 2024, ApJ, 971, 35
Zhang, R., Yuan, H., & Chen, B. 2023, ApJS, 269, 6
Zong, W., Fu, J.-N., De Cat, P., et al. 2018, ApJS, 238, 30